Research Article | Open Access

Microstructures

Singh *et al. Microstructures* **2026**, *6*, 2026058 **DOI:**10.20517/microstructures.2025.129

Exploring Ru/CeO_2 catalysts supported by ceria MOF-derived materials for improved ammonia synthesis and decomposition efficiency at mild conditions

Swati Singh[1,2], Seok-Jin Kim[3], Cafer Tayyar Yavuz[3], Mingwu Tan[4], Eswaravara Prasadarao Komarala[1], Kyriaki Polychronopoulou[1,2]

Keywords:
Ammonia, cracking, metal-organic framework, ceria, metal oxides, catalyst

Citation: Singh, S.; Kim, S. J.; Yavuz, C. T.; Tan, M.; Komarala, E. P.; Polychronopoulou, K. Exploring Ru/CeO_2 catalysts supported by ceria MOF-derived materials for improved ammonia synthesis and decomposition efficiency at mild conditions. *Microstructures* **2026**, *6*, 2026058. https://dx.doi.org/10.20517/microstructures.2025.129

Received: 2 Sep 2025 **First Decision:** 29 Oct 2025 **Revised:** 20 Dec 2025 **Accepted:** 13 Jan 2026 **Published:** 12 May 2026

Academic Editor: Yida Deng **Copy Editor:** Fangling Lan **Production Editor:** Fangling Lan

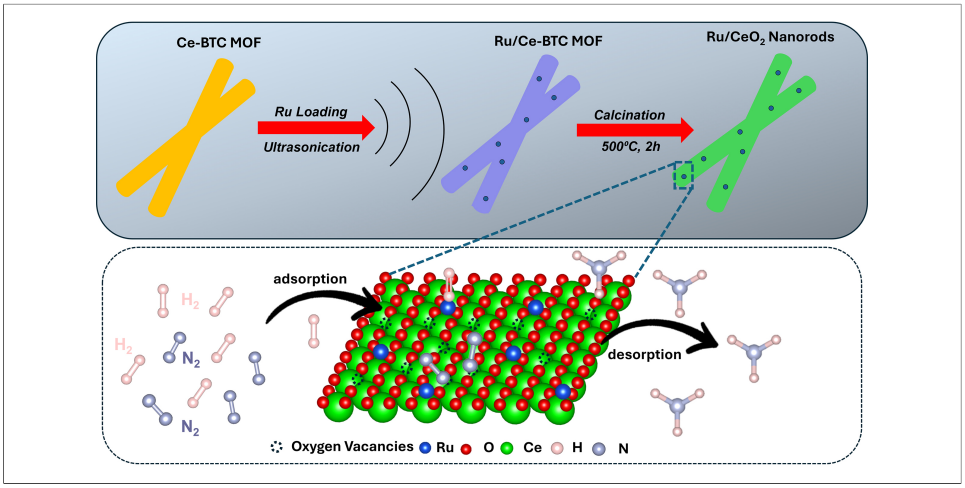

Abstract

Ammonia (NH_3) plays a crucial role in global agriculture and the development of emerging hydrogen energy systems. However, developing highly efficient catalysts for NH_3 synthesis under mild conditions remains a significant challenge due to kinetic and thermodynamic limitations. In this study, we report a Ru/CeO_2 catalyst synthesized using a metal-organic framework (MOF)-derived strategy, which allows for simultaneous control over the morphology of CeO_2 (nanorod shaped), the concentration of oxygen vacancies, and the dispersion of Ru. The optimized catalyst containing 0.5 wt.% Ru delivered an impressive NH_3 synthesis rate of 4,665 μmol $gcat^{-1}$ h^{-1} at 400 °C and 50 bar, while maintaining excellent stability for 45 h of continuous operation. In addition, it achieved a high NH_3 conversion of 93% at 550 °C and 1 bar. Notably, its performance surpasses that of conventional Ru-based catalysts by nearly twofold when normalized to the Ru loading. Comprehensive characterizations, including *in situ* X-ray photoelectron spectroscopy,

[1]Mechanical Engineering Department, Khalifa University, P.O. Box 127788, Abu Dhabi, United Arab Emirates.
[2]Center for Catalysis and Separations (CeCaS), Khalifa University, P.O. Box 127788, Abu Dhabi, United Arab Emirates.
[3]KAUST Catalysis Center, King Abdullah University of Science and Technology, Thuwal 23955-6900, Saudi Arabia.
[4]Institute of Sustainability for Chemicals, Energy and Environment (ISCE2), Agency for Science, Technology and Research (A*STAR), Jurong Island 627833, Singapore.

Correspondence to: Dr. Kyriaki Polychronopoulou, Mechanical Engineering Department, Khalifa University, P.O. Box 127788, Abu Dhabi, United Arab Emirates; Center for Catalysis and Separations (CeCaS), Khalifa University, P.O. Box 127788, Abu Dhabi, United Arab Emirates. E-mail: kyriaki.polychrono@ku.ac.ae

Raman spectroscopy, and scanning transmission electron microscopy, reveal the formation of abundant oxygen vacancies, sub-nanometer Ru clusters, and strong metal support interaction. These factors collectively enhance the activation of N_2 and its hydrogenation. This study highlights the effectiveness of MOF-templated defect engineering in developing robust Ru/CeO_2 catalysts and provides valuable insights into structure-performance relationships. The dual functionality in both NH_3 synthesis and decomposition highlights the potential of this approach for energy-efficient NH_3-based energy systems.

INTRODUCTION

Ammonia (NH_3) is a vital component in fertilizers and various chemicals[1]. Its potential as a renewable energy carrier, thanks to its substantial hydrogen storage capacity (17.6 wt.%) and ease of storage and transportation[2], has recently been recognized. However, the current NH_3 synthesis process, which requires high pressure and temperature (400-500 °C, 20-30 MPa)[3], consumes a significant portion (1%-2%) of global energy annually[4,5]. The high associated costs underscore the need for technological advancements and scale-up of synthesis processes to enhance the NH_3-based economy[5-7]. Therefore, it is imperative to develop a sustainable process for NH_3 production, with the primary challenge being the development of highly active and stable catalysts at mild conditions.

Ceria-based catalysts have demonstrated remarkable efficacy, specificity, and enduring stability across numerous catalytic reactions, marking significant advancements in ceria catalysis technology[8]. Recently, CeO_2 has emerged as a prime candidate for supporting Ru catalysts in NH_3 synthesis, owing to its distinct oxygen storage capacity, Ce^{4+}/Ce^{3+} redox properties, electronic characteristics, and thermal resilience[9-12]. Variations in ceria's morphology, size and heteroatom doping typically impact the formation energy (E_{Ov}) of oxygen vacancies, thus influencing catalytic activity. Additionally, the electronic environment of ceria plays a pivotal role in catalytic performance by altering the metal-support interaction effects[13]. Previous studies[14-18] have shown that the morphology of CeO_2 strongly influences Ru dispersion, oxygen vacancy concentration, and the nature of Ru-Ce interactions, which in turn determine NH_3 synthesis activity. For instance, Ru supported on CeO_2 nanorods exhibited higher activity than nanocubes due to the formation of more oxygen vacancies and smaller Ru species, whereas larger Ru particles on nanocubes led to reduced efficiency[19]. Similarly, morphology-dependent variations in exposed facets and electronic structure of CeO_2 have been linked to significant differences in catalytic performance. Despite these advances, the optimal configuration of Ru species on CeO_2 surfaces for efficient NH_3 synthesis remains unresolved. A major challenge lies in the structural sensitivity of Ru, where only specific active sites (e.g., B5-type step edge sites) are effective for N_2 activation[20]. Conventional preparation methods often produce broad Ru particle size distributions and weak metal-support interactions, limiting atom utilization and stability. Although atomically dispersed Ru or sub-nanoclusters on oxide supports have shown promise[21,22], their controlled synthesis on CeO_2 remains difficult. Thus, the key technical challenge is to develop scalable and precise synthetic strategies that can regulate Ru particle size, dispersion, and interfacial bonding with CeO_2, in order to maximize active site exposure and improve catalytic efficiency[22]. Metal-organic frameworks (MOFs), which consist of metal ions or clusters coordinated by organic ligands, offer a promising solution due to their tunable attributes, such as pore size and geometry, metal composition, breathable framework[23,24]. MOF-derived supports have recently emerged as a powerful approach for designing advanced oxide-supported catalysts with precise control over structural and electronic properties[25]. During the thermal transformation of Ce-based MOFs, the ordered framework decomposes into highly crystalline CeO_2 with preferentially exposed facets (e.g., {111}), while the release of organic linkers simultaneously generates abundant oxygen vacancies. These defects not only enhance the redox capability of CeO_2 but also provide anchoring sites that stabilize sub-nanometer Ru species, thereby strengthening the Ru-Ce interfacial interactions. Moreover, the homogeneous distribution of metal precursors within the MOF lattice enables the formation of well-dispersed Ru nanoparticles with finely

tuned size, preventing aggregation and maximizing metal utilization. Such synergistic regulation of morphology, oxygen vacancy concentration, and Ru dispersion is critical for optimizing N_2 activation and hydrogenation pathways, thereby offering a promising route to high-performance catalysts for ammonia synthesis under mild conditions[26,27].

In this study, catalysts consisting of MOF-derived CeO_2 as the support with varying loadings of Ru metal were developed. Initially, Ceria-MOF and Ru-MOF were prepared and subsequently calcined to yield the Ru/CeO_2 support. The aim was to induce enhanced metal-support interactions. The MOF-derived strategy employed in this work achieves several key effects that have not been realized in previous studies. The complete physicochemical properties of the developed catalysts were explored using various *in-situ* and *ex-situ* characterization techniques, including Inductively Coupled Plasma-Optical Emission Spectroscopy (ICP-OES), X-ray Diffraction (XRD), Raman Spectroscopy, Scanning Electron Microscopy (SEM), N_2-adsorption, High-Resolution Transmission Electron Microscopy (HR-TEM), H_2 Temperature-programmed Reduction (TPR), H_2-Temperature-programmed Desorption (TPD), X-ray photoelectron spectroscopy (XPS). The results of this study demonstrated that the catalysts had an optimal loading of 0.5 wt.% Ru for maximum NH_3 formation rate (4,665 μmol g^{-1} h^{-1} at 400 °C and 50 bar) was achieved at 10,000 mL $g^{-1}h^{-1}$ weight hourly space velocity (WHSV) along with a NH_3 conversation of 93% at 550 °C, 1 bar.

EXPERIMENTAL

Materials

$(Ce(NO_3)_3{\cdot}6H_2O$ > 99%), ruthenium (III) chloride hydrate ($RuCl_3{\cdot}3H_2O$, > 99%), 1,3,5-benzenetricarboxylate (BTC), and ethanol (> 99%), were procured from Sigma-Aldrich and used without further purification; Deionized (DI) water.

Catalyst preparation

Ce-MOF was synthesized following a reported procedure[28] and subsequently calcined at 500 °C to obtain CeO_2. Ru-MOF was prepared via a solvothermal method using $RuCl_3$ and BTC. The XRD [Supplementary Figure 1] and SEM of the prepared Ce-MOF are presented in Supplementary Figure 2A, confirming the successful preparation of Ce-MOF with nanorod morphology. Supplementary Figure 2B shows the SEM of the obtained CeO_2. The *n*Ru/CeO_2 catalysts were synthesized by sonication-assisted mixing of Ce-MOF and Ru-MOF precursors, followed by drying and calcination at 500 °C. Ru loading was varied between 0.2-2 wt.%, and catalysts were denoted as *n*Ru/CeO_2, where *n* represents the Ru content (wt.%). Detailed synthesis procedures are provided in Supplementary Materials.

Characterization

Trace elemental analysis was performed using a Thermo Scientific™ iCAP™ 7600 ICP-OES. Powder XRD was recorded on a X'Pert PRO (Cu Kα, 1.5406 Å, 45 kV, 40 mA) over 2θ = 5°-80° (0.02° step, 10 s/step) using a zero-background holder. Raman spectra were obtained using Witec Alpha 300 RA (532 nm). Surface area and pore distribution were measured on a 3Flex Micromeritics system at 77 K after 8 h degassing at 120 °C (BET and BJH methods). TEM, high-angle annular dark-field (HAADF)-scanning transmission electron microscopy (STEM), and elemental mapping were performed on an FEI TITAN Cs-corrected ChemiSTEM; post-catalysis HR-TEM was acquired on Titan 80-300 ST (300 kV). H_2-TPR and H_2-TPD were conducted on 70 mg of catalyst in a U-tube microreactor (AutoChem 2920). *Ex-situ* XPS was performed on ESCALAB Theta Probe (Al Kα, 1,486.6 eV), calibrated to C 1s (284.8 eV). *In-situ* XRD was carried out on an INEL EQUINOX 3000 with XRK900 reactor under H_2/N_2 (3:1) with stepwise heating to 200-700 °C (1 h per step) and cooling to room temperature (RT). *In-situ* high-resolution XPS was conducted on ULVAC-PHI Genesis 900 under H_2/N_2 (3:1) at RT, 700 °C (2 h), and 400 °C. Full experimental details and characterization data are provided in the Supplementary Materials.

Table 1. Physicochemical properties of *n*Ru/CeO_2 catalysts (*n* = 0.2, 0.5, 1, and 2)

Catalyst before reaction	Ru (wt.%) experimental	Ru[a] (wt.%) ICP-OES	2θ (111)	d-spacing (Å)[b]	Lattice constant *a* (nm)	Crystallite size (nm)[c]	Surface area (m^2/g)	Pore volume (cm^3/g)	Pore diameter (nm)	Intensity ratio ($I_{(598)}/I_{464+1168}$)[d]
CeO_2 support	-	-	29.07	3.069	0.5316	23.9	48	0.13	11	1.02
0.2Ru/CeO_2	0.2	0.22	28.81	3.096	0.5363	28.0	61	0.14	9	1.35
0.5Ru/CeO_2	0.5	0.35	28.97	3.080	0.5334	21.8	72	0.14	8	1.64
1Ru/CeO_2	1	0.41	28.9	3.087	0.5347	21.0	74	0.15	8	1.75
2Ru/CeO_2	2	0.79	28.8	3.097	0.5365	20.5	78	0.13	7	1.84

[a]Values determined by ICP-OES, [b]using Bragg's Law, calculated by (111) facet from XRD patterns for *ex-situ* reduced samples, [c]using Scherrer Equation, [d]using Raman spectroscopy.

Evaluation of catalytic performance

NH_3 synthesis and decomposition assessment

NH_3 synthesis was evaluated in a fixed-bed quartz tube reactor using catalysts diluted with SiC. Reactions were conducted at 400 °C, pressures of 10-50 bar, and a WHSV of 10,000 mL g^{-1} h^{-1} with an N_2/H_2 (1:3) feed. Catalysts were pre-reduced under H_2/N_2 at 800 °C. Helium was used as an internal standard, and outlet NH_3 was quantified online using GC-TCD. NH_3 decomposition was performed in the same reactor after reduction at 700 °C under H_2/N_2. Measurements were carried out at a WHSV of 24,000 mL g^{-1} h^{-1} over a temperature range of 350-550 °C, with NH_3 as the feed gas and He as an internal standard. Each experiment was repeated thrice.

Stability of NH_3 synthesis activity test

Catalyst stability was assessed under continuous NH_3 synthesis conditions at 400 °C and 50 bar for 45 h following reduction at 800 °C. NH_3 concentration in the outlet stream was continuously monitored to evaluate long-term performance. Each experiment was repeated thrice. Full experimental procedures and operating details are provided in the Supplementary Materials.

RESULTS AND DISCUSSION

Elemental composition and morphology of the prepared catalysts

The Ru content in the as-synthesized catalysts, prepared via the MOF-derived method described in Section "Materials", was quantified using ICP-OES. The actual Ru compositions are provided in Table 1. Across all samples, the measured Ru content was slightly lower than the nominal loading, which is consistent with known losses due to the volatility of ruthenium oxides during thermal treatment[29]. Previous studies[28-30] have reported that CeO_2 can interact strongly with RuO_x species, effectively stabilizing them and minimizing their volatilization compared to other oxide supports. In line with this, the ICP-OES data reveal minimal Ru loss for the 0.2Ru/CeO_2 and 0.5Ru/CeO_2 catalysts, especially at lower loadings. This suggests that stronger metal-support interactions may occur at reduced Ru content, enhancing the retention of Ru during synthesis. SEM analysis [Supplementary Figure 3A-C] revealed that the Ce-MOF-derived CeO_2 support consists of interwoven nanorods (100-200 nm in diameter, 1-2 μm in length) forming a fibrillar network[31]. After calcination at 500 °C, the rod-like morphology is largely preserved, indicating strong shape inheritance from the Ce-MOF precursor. Ru deposition (0.2-1 wt.%) does not alter the primary ceria morphology; the nanorods remain cross-linked with open interparticle voids. At higher Ru loadings (0.5-1 wt.%), slight bundle thickening and local necking are observed, but no Ru agglomerates are detected, suggesting high Ru dispersion. The preserved open rod-based framework provides short diffusion paths, mechanical stability,

and high external surface area, which are favorable for catalysis and consistent with previous reports[30-32].

Structural and textural study of Ce MOF-derived supported catalysts

Supplementary Figure 4 displays the XRD patterns of the as-prepared CeO_2 supports and their corresponding *n*Ru/CeO_2 catalysts. Figure 1A shows the XRD patterns of the *ex-situ* reduced (under H_2/Ar at 700 °C) catalysts, revealing the characteristic planes of CeO_2 as observed for the fresh catalysts with enhanced crystallinity across the board. The diffraction peaks observed at 28.7°, 33.3°,47.7°, 56.5°, 59.4°, 69.7°, 76.9°, and 79.3° correspond to the CeO_2 (111), (200), (220), (311), (222), (331), (420), and (422) planes, respectively. However, when compared, it was noted that crystallinity decreases as the Ru loading increases, along with slight peak broadening. The decrease in crystallinity with increased Ru loading is often due to the introduction of structural disorder (defects), formation of amorphous phases, or interference with the host material's crystal lattice[33,34]. These effects are typically more pronounced at higher loadings, where the influence of Ru on the material's structure becomes more significant, suggesting that the doping of Ru species could suppress the crystallinity of CeO_2, probably due to the substitution of Ce^{4+} (0.97 Å) in CeO_2 by Ru ions with a smaller radius (< 0.7 Å)[35]. The crystallite size of fluorite CeO_2 support and *n*Ru/CeO_2 catalysts were in the range of 21-28 nm. The calculated lattice parameters for CeO_2 support and the Ru-loaded CeO_2 catalysts were 5.316 Å (CeO_2), 5.3363 Å (0.2Ru/CeO_2), 5.334 Å (0.5Ru/CeO_2), 5.347 Å (1Ru/CeO_2), and 5.365 Å (2Ru/CeO_2). Interestingly, this slight expansion of the lattice with Ru incorporation appears counterintuitive, given that Ru^{4+} (ionic radius ~0.64 Å, 6-fold coordination) is smaller than Ce^{4+} (0.97 Å, 8-fold coordination)[36], which would typically lead to lattice contraction. Nevertheless, similar trends have been reported in previous studies, where Ru incorporation led to lattice expansion, likely due to structural distortions or defect formation[37,38]. To further support this observation, Raman spectroscopy was employed, discussed below in detail. CeO_2, with its fluorite-type cubic structure, normally exhibits a prominent Raman band corresponding to the F_{2g} symmetric oxygen breathing mode. Upon Ru addition, this peak was found to shift slightly toward lower wavenumbers (459.7 cm^{-1}), providing additional evidence for lattice expansion caused by Ru substitution[39]. The N_2 adsorption/desorption and pore-size distribution of the as-prepared CeO_2 supports, and the corresponding *n*Ru/CeO_2 catalysts are shown in Figure 1B and C, respectively. The N_2 adsorption/desorption shows that both the CeO_2 supports and the corresponding *n*Ru/CeO_2 catalysts exhibit a typical type IV adsorption isotherm, with a clear H3-type hysteresis loop appearing between p/p_0 = 0.6 and 1.0, suggesting that the CeO_2 supports and *n*Ru/CeO_2 catalysts possess a mesoporous structure. Additionally, there is an increase in the N_2 adsorption at higher pressures, indicating the presence of macropores within the CeO_2 support. The BET surface area, pore diameter, and pore volume of the samples are provided in Table 1. The BET specific surface areas of the catalysts, ranging from 48 to 74 m^2/g, are in good agreement with values reported in the literature for similar CeO_2-based materials[40-43]. The observed increase in surface area following Ru impregnation and subsequent thermal treatment is likely due to surface modifications of CeO_2 that create or expose additional interparticle voids, thereby enhancing N_2 adsorption capacity[44]. The increase in surface area with increasing Ru loading could also be due to the possible formation of surface defects (O vacancies)[45]. High defect content is beneficial to generate a high specific surface area, as also observed by Zhou *et al.*[46], where they observed increasing surface area with increasing defect density within the Ce MOF structure.

In-situ XRD (structural properties)

For the *n*Ru/CeO_2 catalysts, XRD analysis was conducted under controlled reduction conditions to monitor structural changes in the 200-800 °C temperature range. The initial XRD measurement was performed at RT. The catalyst was then heated up to 200 °C and held for 1 h under a reducing gas mixture atmosphere (H_2/N_2 = 3:1), followed by the acquisition of the XRD measurement. This process was repeated sequentially at 400, 600, and 700 °C, with each temperature maintained for 1 h before collecting the XRD measurements. After the final step at 700 °C, the catalyst was cooled down to RT under the same reducing atmosphere, and a final

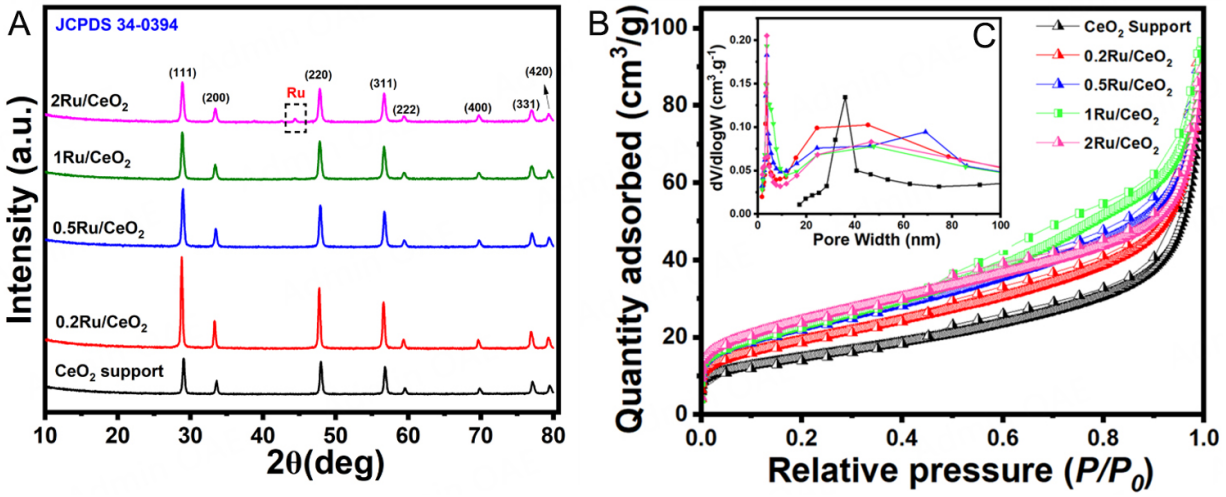

Figure 1. (A) XRD profile of reduced (under 10% H_2/Ar, at 700 °C), CeO_2 support and *n*Ru/CeO_2 catalysts, (B) N_2 adsorption-desorption isotherms, (C) inset shows the pore size distribution), obtained at 77 K of the as-prepared CeO_2 support and *n*Ru/CeO_2 catalysts (*n* = 0.2, 0.5, 1, and 2).

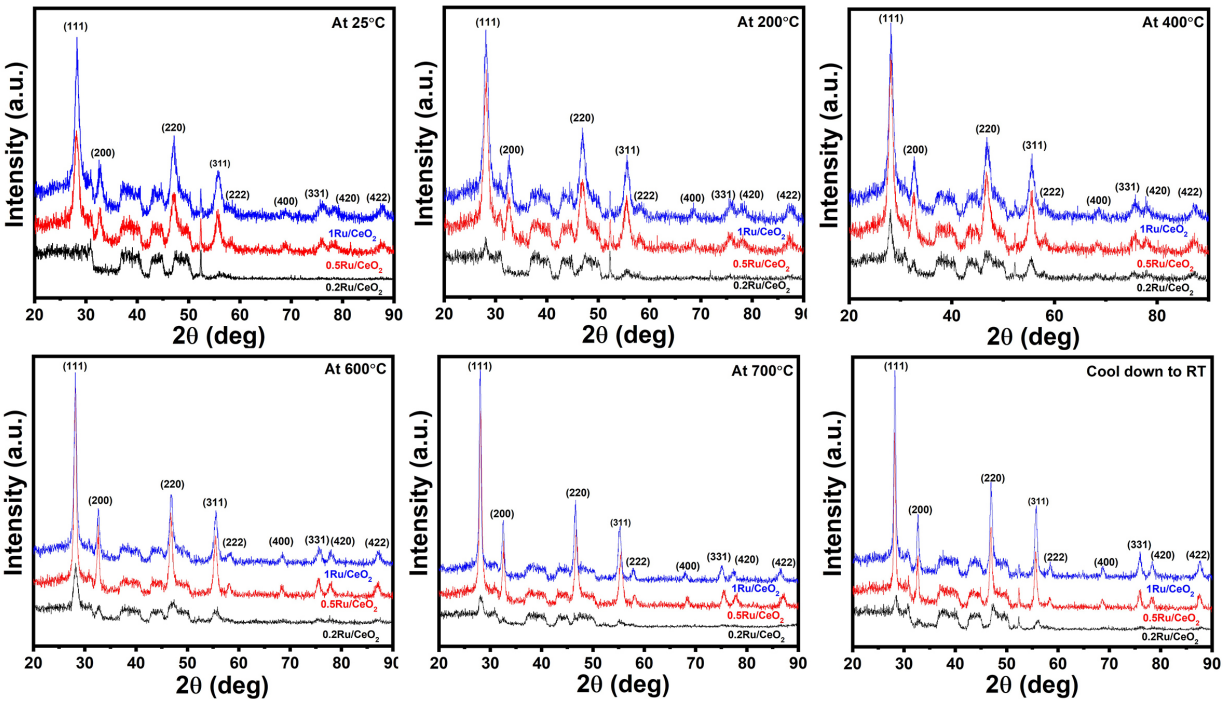

Figure 2. *In-situ* XRD patterns of the nRu-CeO_2 catalysts, *n* = 0.2, 0.5, 1 at 25 °C (atmospheric), 200 °C, 400 °C, 600 °C, 700 °C (reduction, H_2/N_2 = 3:1), and after cooling to RT. CeO_2 reflections are indexed.

XRD analysis was performed to assess any post-reduction structural changes. As observed from Figure 2, the XRD peaks of the catalysts exhibit no changes in the characteristic CeO_2 diffraction peaks under atmospheric conditions or with increasing temperatures during reduction atmosphere, apart from an improvement in crystallinity. Notably, no Ru-related peaks are observed in the *in-situ* XRD patterns. This absence is attributed to the exceptionally small Ru particle size, determined to be less than 1.5 nm by HR-TEM, which falls below the detection limit of XRD analysis. Additionally, HR-TEM analysis (discussed below) confirmed the uniform dispersion of Ru nanoparticles across the catalyst surface, further explaining the absence of distinct Ru peaks in the *in-situ* XRD results.

Raman studies

Oxygen vacancies (O_{Vs}) are widely recognized as crucial descriptor for catalytic activity, as they not only lower the activation energy barrier for N_2 adsorption but also serve as active reaction sites. To investigate these defect sites, Raman spectroscopy was employed on *ex-situ* reduced (under H_2/Ar at 700 °C) catalysts, as illustrated in Figure 3. The Raman spectra of CeO_2 primarily feature a prominent F_{2g} band at 465.3 cm^{-1}, characteristic of the fluorite phase. Additionally, weaker bands are observed at 257, 598, and 1,172 cm^{-1}, which are attributed to the second-order transverse acoustic (2TA) mode, defect-induced (D) mode, and second-order longitudinal optical (2LO) mode, respectively[47-49]. A sharp and symmetric F_2g band at ~465.3 cm^{-1} indicates high crystallinity and a well-ordered fluorite structure, also observed from XRD results above. In addition, the incorporation of Ru metal causes a noticeable red-shift and broadening of the F_2g vibrational band. The shift to 465.3 cm^{-1}, accompanied by band broadening, suggests alterations in the Ce-O bonding environment due to Ru interaction, an effect that aligns with observations reported by Giri *et al.*[47], indicating that the deposited Ru lowers the symmetry of the Ce-O bond, by introducing O_{Vs} and Ru-Ce-O bond formation[47]. It has been reported that for pure RuO_2, bands at 528, 644, and 716 cm^{-1}, corresponding to the E_g, A_{1g}, and B_2g modes, are typically observed[50]. However, these bands have low intensity relative to the CeO_2 bands and are not detectable in the Ru/CeO_2 spectra. This is likely due to the small amount of Ru present or the interaction between the Ru species and ceria, as supported by the XRD results. The I_D-to-I_{F2g} ratios, specifically $I_{(598+1172)}/I_{465.3}$, which reflect intrinsic defect concentrations such as oxygen vacancies (O_V)[51], are summarized in Table 1. The CeO_2 support synthesized in this study exhibited a notably higher ratio compared to CeO_2 supports reported in the literature, implying an oxygen vacancies abundance. This enhanced defect density is attributed to the unique synthesis route involving Ce-MOFs, which offers a more porous structure conducive to O_V formation. Notably, a previous study reported $I_{(1175+600)}/I_{462}$ ratios of only 0.07 and 0.04 for CeO_2-rod and CeO_2-cube, respectively, indicating low vacancy levels, while their corresponding Ru-loaded counterparts (Ru/CeO_2-r and Ru/CeO_2-c) showed slightly elevated ratios of 0.40 and 0.31[14]. In contrast, the present work exhibits systematically higher $I_{(598+1172)}/I_{465.3}$ ratios, increasing with Ru loading from 1.02 (CeO_2) to 1.35 (0.2Ru/CeO_2), 1.64 (0.5Ru/CeO_2), 1.75 (1Ru/CeO_2), and 1.84 (2Ru/CeO_2). This underscores the enhanced O_V population due to both the preparation strategy and the synergistic effect of Ru incorporation. In our work, the CeO_2 support exhibits a characteristic peak at {111}, which aligns with the theoretical calculations that indicate oxygen vacancy formation energies vary with the exposed crystal plane in the order {110} < {100} < {111}[52,53]. The presence of this peak at {111} suggests that oxygen vacancies are effectively created on this plane, supporting the higher formation energy of vacancies observed for the {111} plane. This confirms that the {111} plane is more favorable for oxygen vacancy formation, as seen in our experimental results, where the catalytic activity is enhanced due to the presence of these vacancies. Moreover, DFT studies suggest that Ru dopants activate lattice oxygen by elongating Ce-O and Ru-O bond[54], lengths relative to their parent oxides, thereby facilitating O_v generation by acting as nucleation centers for O_V clusters on CeO_2 surfaces[55].

Reduction behavior

To gain deeper insight into the metal-support interactions and redox characteristics of the synthesized catalysts, H_2-TPR was conducted over the 35-800 °C temperature range of [Figure 4A]. H_2-TPR profiles of *n*Ru/CeO_2 catalysts exhibit a prominent low-temperature reduction peak in Region I (~50-150 °C) corresponding to the reduction of RuO_2 to Ru, which shifts to lower temperatures with increasing Ru loading[56]. In contrast, the surface reduction peak of CeO_2 in Region II (150-500 °C) appears less pronounced in *n*Ru/CeO_2 catalysts compared to pure CeO_2[57]. Additionally, the bulk CeO_2 reduction Region III (> 500 °C) is significantly suppressed in Ru-containing catalysts[58]. The downward shift of the RuO_2 reduction peak (observed around 50-150 °C) with increasing Ru loading from 0.2 to 0.5 wt.% indicates improved reducibility of the catalyst. This behavior suggests that Ru nanoparticles are highly dispersed at the atomic scale, as confirmed by HRTEM, where the particle size is below 1.5 nm. The distribution of active components on the

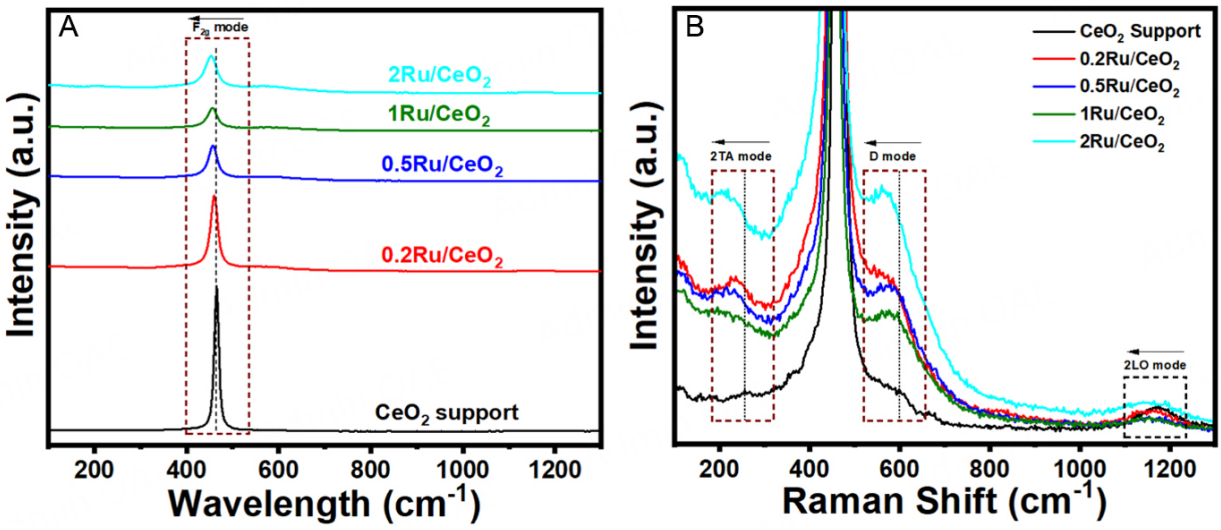

Figure 3. Raman spectra of CeO_2 support and *n*Ru/CeO_2 (*n* = 0.2, 0.5, 1, and 2). (A) zoomed-out region, and (B) zoomed-in region.

catalyst surface plays a crucial role in the reduction of surface oxygen. With higher dispersion of Ru metal, hydrogen activation is facilitated more efficiently, leading to an increase in H_2 consumption[59]. Such fine dispersion promotes hydrogen spillover[60,61], enabling H_2 to dissociatively chemisorbed and migrate onto the CeO_2 support more effectively. As the Ru loading increases from 0.2 to 0.5 wt%, a greater number of well-dispersed Ru species become available, enhancing the overall reduction process at lower temperatures. In case of 1Ru/CeO_2 catalyst, two step reduction of RuO_2 happens (observed around 50-150 °C), leading to the formation of RuO and Ru species. The multiple reduction peaks in H_2-TPR profiles of 1RuO_2/CeO_2 catalysts can be attributed to different RuO_2 particle sizes[62,63] and their varying interactions with the support, as seen in HRTEM where some larger Ru nanoparticles were observed. The weaker CeO_2 surface reduction in *n*Ru/CeO_2 implies that Ru promotes Ov formation at lower temperatures, leading to a more gradual, extended reduction. More surface oxygen is removed below 150 °C, generating abundant Ov compared to bare CeO_2, likely via hydrogen spillover[64-66]. Among the samples, 0.5Ru/CeO_2 shows the most favorable reduction profile, suggesting easier Ov formation. Enhanced oxygen vacancies facilitate N_2 dissociation[67-69], improving NH_3 synthesis performance.

Metal dispersion

The H_2-TPD analysis of the *n*Ru/CeO_2 catalysts shown in Figure 4B revealed two distinct regions. Region I corresponds to the weakly adsorbed H-species on highly dispersed Ru nanoclusters with two different H adsorption sites observed: one on Ru metallic sites of varying sizes. Region II corresponds to the strongly adsorbed dissociative H-species that are taken up by the Ru-CeO_2 metal-support interface, which is closely associated with oxygen vacancies on the CeO_2 support. In the higher temperature range (150-350 °C), the peak associated with strongly adsorbed hydrogen on Ru-CeO_2 interfaces or O vacancies showed a slight increase in intensity with higher Ru loading. This suggests the increase in O vacancies along with enhanced hydrogen spillover from Ru to CeO_2 with increased Ru loading, leading to more hydrogen being stored and subsequently desorbed from these interfacial sites. The crystallite sizes [Supplementary Table 1] obtained from the H_2-TPD analysis are provided in Supplementary Materials.

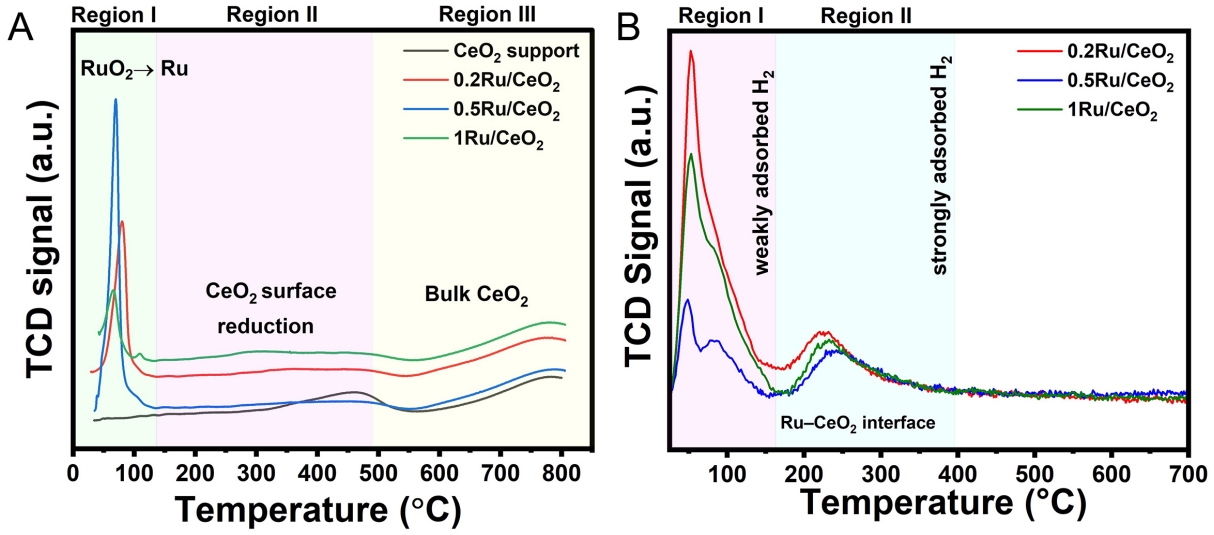

Figure 4. (A) H_2-TPR profile of CeO_2 support and *n*Ru/CeO_2 catalysts (*n* = 0.2, 0.5, and 1), (B) H_2-TPD profile of *n*Ru/CeO_2 catalysts (*n* = 0.2, 0.5, and 1).

Ex-situ XPS for surface analysis

To gain a clearer understanding of the oxidation states and local environment of Ru species, XPS was performed on the catalysts following *ex-situ* reduction in H_2/Ar at 700 °C. This analysis primarily aimed to evaluate the extent of Ru reduction and the interaction between Ru and the CeO_2 support. The Ru 3p peaks at 461.9 and 484.1 eV are indicative of metallic Ru, whereas those at 463.7 and 485.9 eV correspond to oxidized Ru in the form of RuO_2, as previously reported by Wang *et al.*[70]. Deconvolution of Ru 3p signals was carried out using Shirley background correction, revealing distinct electronic environments for the different loadings, and is shown in Figure 5A-C. The 0.5Ru/CeO_2 catalyst predominantly exhibited metallic Ru, with characteristic peaks at 461.8 and 484.3 eV. In contrast, 0.2Ru/CeO_2 and 1Ru/CeO_2 catalysts showed a noticeable shift toward higher binding energies (463.1/485.3 eV and 462.4/484.7 eV, respectively), suggesting a greater proportion of oxidized Ru species (Ru^{4+}). This shift likely arises from variations in the chemical surroundings or electron transfer between Ru and the CeO_2 support, thus driving the Ru oxidation state and of the SMSI phenomena between Ru and ceria support.

The O 1s XPS spectra [Figure 5D-F] revealed three distinct oxygen environments in all three catalysts under study. The peak at ~528.8 eV corresponds to lattice oxygen (O_L), while those around ~530 and 532-533 eV are attributed to oxygen vacancies (O_v) and surface species such as hydroxyls or carbonates, respectively[71]. Deconvolution using Shirley background correction showed peaks at 528.4, 530.1, and 532.0 eV for 0.2Ru/CeO_2, 528.8, 530.9, and 532.8 eV for 0.5Ru/CeO_2, and 528.4, 530.1, and 532.0 eV for 1Ru/CeO_2. Notably, the 0.5Ru/CeO_2 catalyst exhibited a comparatively lower intensity of carbonate-related peaks. The reduced presence of carbonate species is beneficial, as it implies fewer surface-blocking contaminants, thereby exposing more catalytically active sites. This cleaner surface enhances metal-support interactions and facilitates the formation and preservation of oxygen vacancies, both of which are critical for promoting N_2 activation and hydrogen dissociation. Moreover, a lower population of carbonates also contributes to improve surface basicity and support reducibility, ultimately leading to superior catalytic performance of 0.5Ru/CeO_2 in NH_3 synthesis under mild reaction conditions.

The Ce 3d XPS spectra shown in Figure 5G-I display a complex pattern, characteristic of cerium oxide, and have been deconvoluted based on established literature assignments[72-74]. The spectral features at ~915.4, 906.4, 899.7, 897.1, 887.4, 881.3 eV correspond to the presence of Ce^{4+} oxidation states. In contrast, the peaks

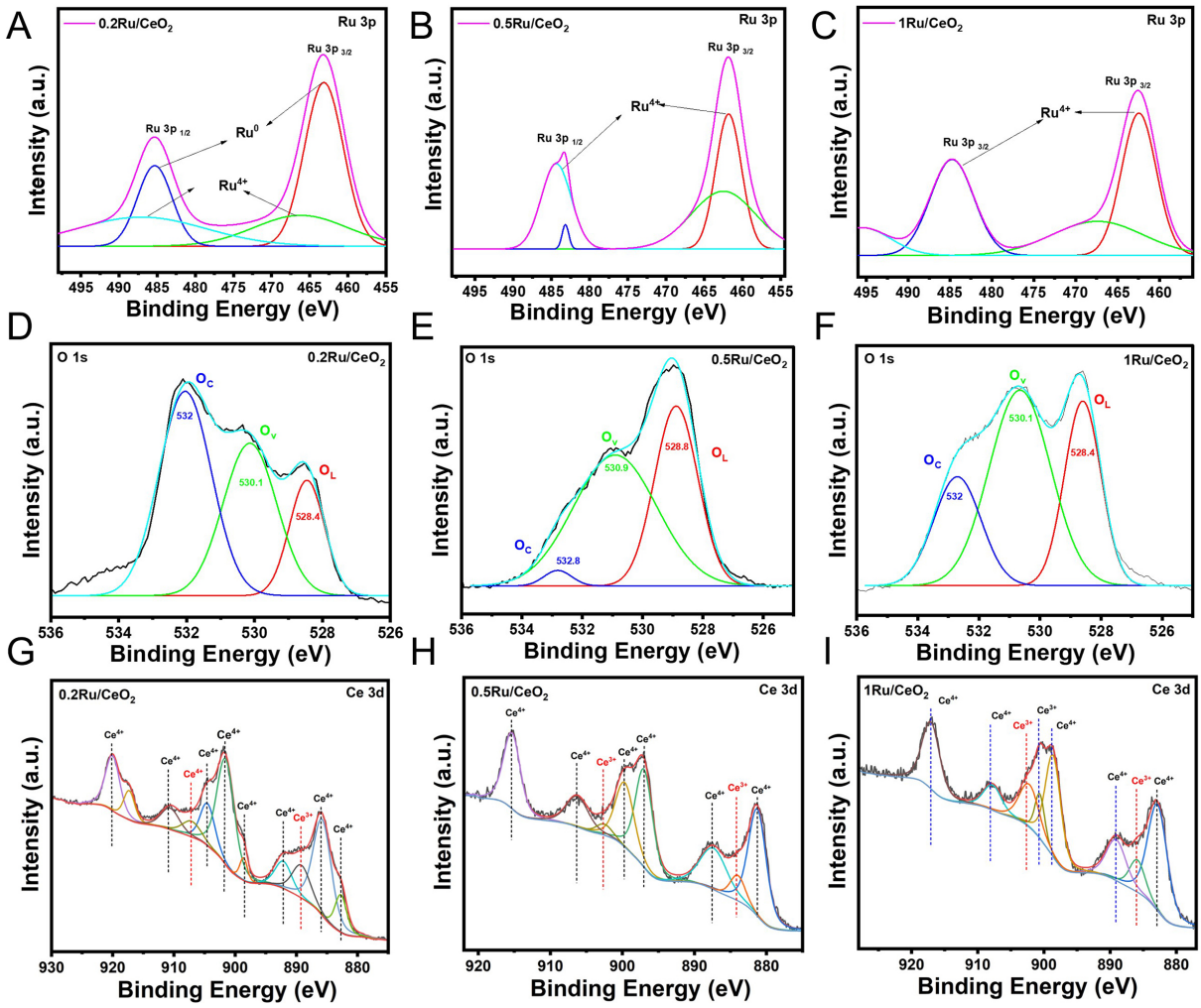

Figure 5. Deconvoluted XPS spectra of (A-C) Ru 3p, (D-F) O 1s, and (G-I) Ce 3d XPS core-level spectra of *ex-situ* reduced (under H_2/Ar at 700 °C) *n*Ru/CeO_2 catalysts (*n* = 0.2, 0.5, and 1).

centered around 902.6 and 884.1 eV are attributed to the presence of Ce^{3+} species, indicating the partial reduction of cerium within the oxide lattice.

In-situ XPS (surface atomic%)

An *in-situ* XPS study was performed to examine the surface composition of the catalysts under different conditions. XPS spectra were collected for fresh samples at RT, after reduction in N_2/H_2 (1:3) at 700 °C for 2 h, and under reaction conditions at 400 °C. Supplementary Figures 5-7 show the corresponding core-level XPS spectra of the *n*Ru/CeO_2 catalysts (*n* = 0.2, 0.5, and 1), provided in the Supplementary Materials.

The reduction process performed under the N_2/H_2 atmosphere significantly impacts the surface composition trends of the *n*Ru/CeO_2 catalysts as presented in Table 2. Initially, at 25 °C, the catalysts exhibit a lower atomic% of Ru and varying amounts of Ce and O, reflective of the as-synthesized state of catalysts before reduction. As the temperature increases to 700 °C (reduction condition), the Ru atomic percentage rises notably, indicating that the reducing environment promotes Ru migration toward the surface and enhances its dispersion on the ceria support. This trend is further corroborated by XPS analysis, which reveals a temperature-dependent increase in the surface Ru/Ce ratio accompanied by a decrease in the O/Ce ratio, evidencing Ru surface enrichment and partial reduction of CeO_2 to CeO_{2-x} [75]. The resulting Ru-rich,

Table 2. Surface compositions of *n*Ru/CeO_2 catalysts (*n* = 0.2, 0.5, and 1)

Catalysts	Temperature (°C)	Ru (atomic%)	Ce (atomic%)	O (atomic%)	O/Ce	Ru/Ce
0.2Ru/CeO_2	25	0.24	31.33	68.98	2.22	0.0076
	700	0.30	34.39	65.31	1.89	0.0087
	400	0.30	34.44	65.26	1.89	0.0087
0.5Ru/CeO_2	25	0.35	34.27	65.39	1.90	0.0102
	700	0.64	35.74	63.62	1.78	0.0179
	400	0.57	36.87	62.56	1.77	0.0154
1Ru/CeO_2	25	0.49	33.68	65.84	1.95	0.0145
	700	1.09	36.38	62.53	1.72	0.0299
	400	0.82	35.49	63.68	1.79	0.0231

oxygen-deficient surface provides an optimal population of Ru-CeO_{2-x} interfacial sites. The elevated temperature likely enhances the reduction of both Ru and CeO_2, facilitating an interaction between metal and support that stabilizes Ru in a metallic form, which is often more catalytically active. After this step, when the temperature is reduced back to 400 °C (reaction condition), the atomic% of Ru remains almost similar with a slight reduction. This suggests that the stability of Ru on the surface is maintained after the reduction.

Moreover, oxygen vacancies (O_v)[76-78] are prevalent anionic point defects commonly observed in transition and f-block metal oxides. These vacancies typically arise in materials containing cations that can alternate between multiple oxidation states, such as Ce^{3+}/Ce^{4+}[77,79,80] and Ti^{3+}/Ti^{4+}[81]. The formation of Ov is often induced by high-temperature treatments[82] or under reducing environments[83], where lattice or surface O^{2-} ions are removed alongside the reduction of metal cations, all while preserving the overall crystal framework. Such defect sites are particularly significant in the context of heterogeneous catalysis[77,79,80]. In the case of CeO_2, which adopts a cubic fluorite structure (space group *Fm*$$\overline{3}$$*m*), the introduction of O_v is associated with the partial reduction of Ce^{4+} to Ce^{3+}. This process modifies the surface electronic environment and introduces positively charged sites[84], which are known to enhance catalytic activities in reactions like NH_3 synthesis, CO oxidation, the water-gas shift reaction, and CO_2 conversion[3,77,78].

At ambient conditions (25 °C), the surface environment of the catalyst shows an O/Ce ratio close to 2, indicating a well-oxidized surface (where O_v population is expected to be low)[85]. However, under reducing conditions, the O/Ce ratio decreases to ~1.7 signifying the removal of O atoms from the lattice, thus leading to the formation of O vacancies (CeO_{2-x}). In the case of 0.5Ru/CeO_2, most O_v (O/Ce = 1.77) was observed at the reaction condition (400 °C) as compared to the rest of the catalysts. These vacancies play a critical role in enhancing catalytic performance by serving as active sites and improving the mobility of lattice oxygen for redox reactions[86]. Additionally, the removal of oxygen reduces Ce^{4+} to Ce^{3+}, altering the electronic environment and influencing the adsorption and activation of reactants[87]. The formation of O vacancies also induces slight lattice distortions, which can enhance interactions with other species, such as Ru in the *n*Ru/CeO_2 catalysts[88]. This demonstrates the importance of the reducible nature of CeO_2 in enabling its superior catalytic activity under reaction conditions as discussed below.

HR-TEM microstructural studies

HR-TEM was carried out on the reduced catalysts to examine their microstructure and elemental distribution under reaction conditions. The HRTEM images shown in Supplementary Figure 8 reveal that all three catalysts exhibit a rod-like structure with elongated particles. This suggests a distinct morphology of the *n*Ru/CeO_2 catalyst system, likely influenced by the MOF-derived preparation method.

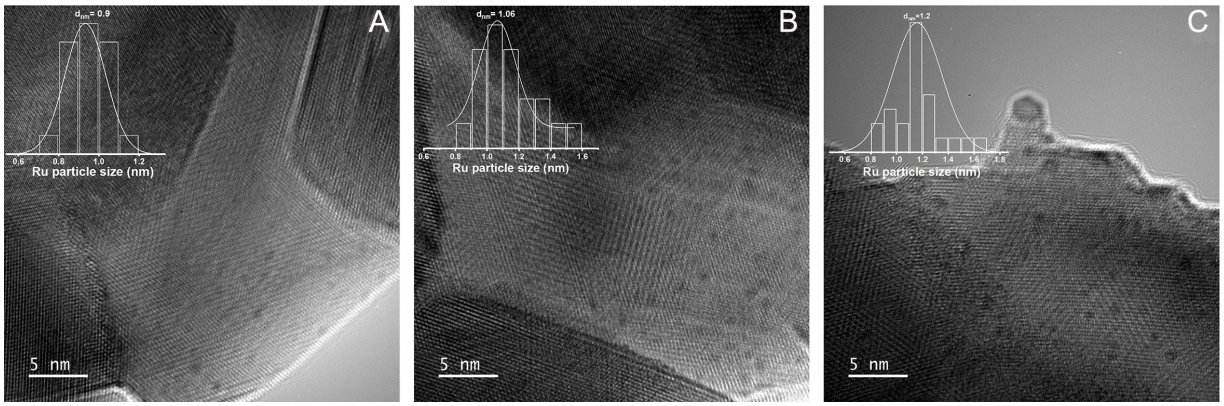

Figure 6. HR-TEM micrographs of (A) 0.2Ru/CeO_2, (B) 0.5Ru/CeO_2, and (C) 1Ru/CeO_2. The inset contains particle size distribution.

Figure 6A-C present the HRTEM images of the *n*Ru/CeO_2 catalysts. The inset in each image shows the Ru particle size distribution, which indicates an increase in particle size across the three catalysts. Specifically, the particle sizes range from 0.9 to 1.06 to 1.2 nm as the n values increase from 0.2 to 0.5, and then to 1, respectively. This indicates a clear relationship between Ru loading and particle size growth, as anticipated. Additionally, good dispersion of Ru was observed for all three *n*Ru/CeO_2 catalysts. However, at a Ru loading of 1 wt.%, slight agglomeration of Ru was observed, particularly at the edges of the surface. This agglomeration can be attributed to the high surface energy of Ru (~2.5-3.0 J/m^2) at the edges, which promotes particle growth as a way to minimize surface energy (J/m^2)[89]. Moreover, HR-TEM images of the reduced 0.5Ru/CeO_2 catalyst [Supplementary Figure 9A-C] show lattice fringes indexed to the CeO_2 (220) and (111) planes, with *d*-spacings of ~0.19 and ~0.32 nm, respectively. The corresponding FFT patterns (insets) are consistent with a retained CeO_2 fluorite structure after reduction.

Elemental mapping [Figure 7] further confirmed the distribution of elements (Ce, Ru, and O) across the *n*Ru/CeO_2 catalysts. The mapping data showed that Ru is homogeneously dispersed throughout the catalyst, providing evidence of uniform distribution even at varying Ru loadings in the range studied. These findings highlight the interplay between Ru loading, particle size, and dispersion characteristics, which are critical for catalytic interface and performance afterall.

To critically evaluate the MOF-derived catalyst, Figure 8 compares HR-TEM images and Ru particle size distributions of 0.5Ru/CeO_2 catalysts prepared using MOF-derived CeO_2 and commercial CeO_2 supports. The MOF-derived catalyst exhibits well-defined nanorod morphology and uniformly dispersed Ru nanoparticles with a smaller average size (d_{avg} ≈ 1.06 nm), whereas the commercial CeO_2-based catalyst shows no distinct morphology and significantly larger, less uniform Ru particles (d_{avg} ≈ 3.7 nm). The nanorod structure formed via MOF templating enhances Ru dispersion due to higher surface area, abundant oxygen vacancies, and exposure of reactive {111} and {100} facets, which promote strong metal-support interactions and suppress Ru sintering. These features provide a higher density of active sites for N_2 activation, favoring NH_3 synthesis, consistent with previous reports highlighting the superior performance of Ru/CeO_2 nanorods over other morphologies[90,91].

Catalysts' assessment towards NH_3 synthesis

CeO_2 is widely used in catalysis for its Ce^{4+}/Ce^{3+} redox behavior, oxygen storage capacity, and electronic structure, which promote NH_3 synthesis by creating oxygen vacancies (Ov) and modulating Ru species[19,92,93]. Beyond reduction behavior, CeO_2 morphology, Ru loading, and dispersion strongly influence catalytic performance. Nanorods and polyhedrons enhance activity by providing high surface area, abundant Ov, and

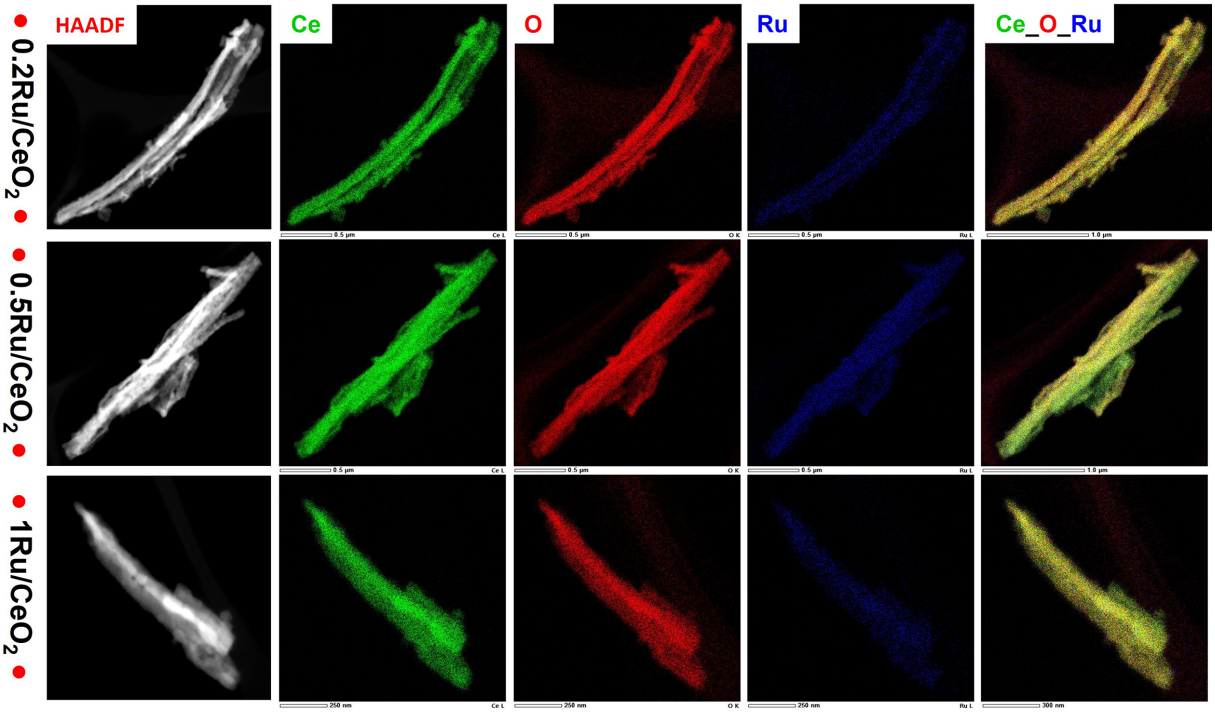

Figure 7. STEM-HAADF image and elemental mapping of the selected area of *n*Ru/CeO_2, *n* = 0.2, 0.5, and 1wt.%. Ce (Green), O (Red), Ru (Blue), Ce-O-Ru (GRB).

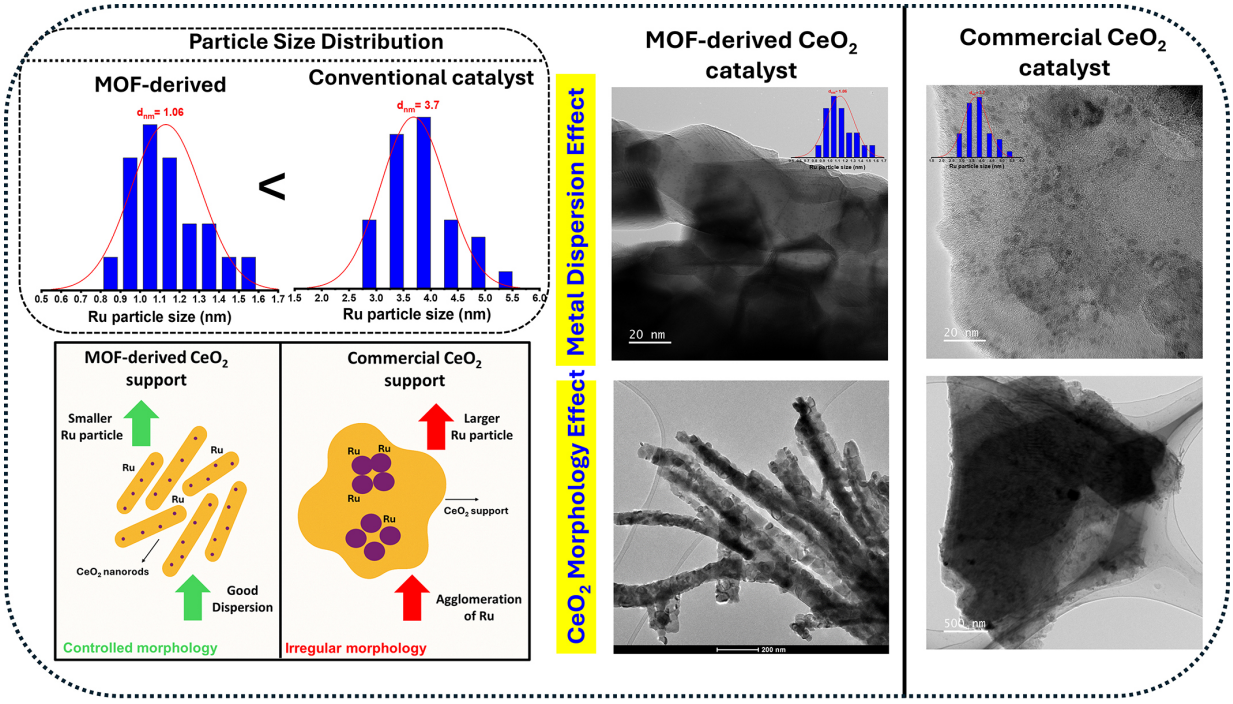

Figure 8. Comparative schematics of MOF-derived support and commercial CeO_2, particle size distribution (left) and CeO_2 morphology/metal dispersion (right) effect of 0.5Ru/CeO_2 catalyst prepared via MOF-derived CeO_2 and commercial CeO_2 .

exposed {111}/{100} facets, which stabilize small, low-crystallinity Ru species with higher surface Ru^{4+}, whereas nanocubes form larger, poorly dispersed Ru particles with weaker metal-support interactions[19,90,94]. Ru-O-Ce linkages further generate Ov via partial Ce^{4+} reduction, facilitating H_2 and N_2 adsorption and N_2

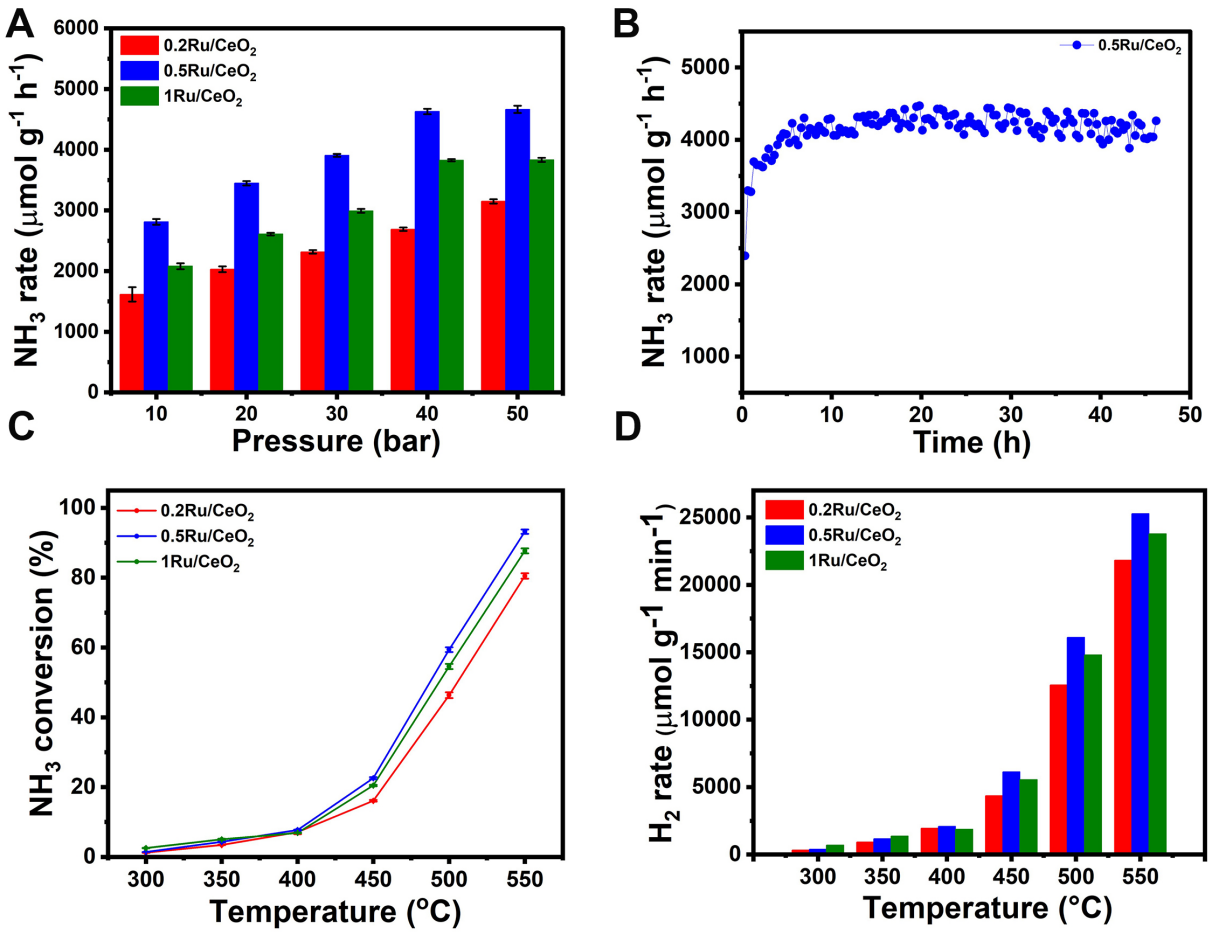

Figure 9. (A) The NH_3 synthesis rate of *n*Ru/CeO_2 catalysts (*n* = 0.2, 0.5, and 1) at 400 °C, 10,000 mL $g^{-1}h^{-1}$ WHSV and different pressure ranges (10-50 bar), (B) Stability test of 0.5Ru/CeO_2 catalyst at 50 bar, 400 °C, and 10,000 mL $g^{-1}h^{-1}$, (C) NH_3 decomposition conversion graph with respect to temperature, at *P* = 1 atm, *T* = 350-550 °C, and (D) H_2 production rate (mmol g^{-1} min^{-1}) with respect to temperature, at *P* = 1 atm, *T* = 350-550 °C. (A and C) represent the standard error of the mean (SEM).

dissociation, a rate-limiting step in NH_3 formation[95,96]. Similar effects of Ov on N_2 activation have been observed in photocatalytic systems such as BiOBr[97], TiO_2 [98], and TiO_2/Au nanorods[99], highlighting the critical role of oxygen-deficient sites. The NH_3 synthesis of *n*Ru/CeO_2 catalysts (*n* = 0.2, 0.5, 1) was evaluated using a 25% N_2-75% H_2 feed. Figure 9 and Supplementary Table 2 illustrate the NH_3 synthesis rates at 400 °C across a pressure range of 10-50 bar for the CeO_2 support and *n*Ru/CeO_2 catalysts.

CeO_2 morphology effect

The MOF-derived CeO_2 support was evaluated for NH_3 synthesis across varying pressures. It remained largely inactive at 10-20 bar but showed noticeable activity at higher pressures, achieving an NH_3 yield of 374 μmol g^{-1} h^{-1} at 400 °C and 50 bar [Supplementary Table 2]. This activity is attributed to CeO_2's redox properties, which generate oxygen vacancies (Ov) crucial for N_2 activation, and its nanorod morphology, which exposes reactive facets and increases Ov density. Ma *et al.*[19] reported similar trends, where Ru/r-CeO_2 exhibited a higher reaction rate (3,830 μmol g^{-1} h^{-1} at 400 °C) compared to Ru/p-CeO_2 (529 μmol g^{-1} h^{-1}) and Ru/c-CeO_2 (1,289 μmol g^{-1} h^{-1}). A control 0.5Ru/CeO_2 catalyst prepared using commercial CeO_2 showed negligible activity under identical conditions. This contrast confirms that the enhanced performance of MOF-derived CeO_2 arises from its nanorod morphology, higher Ov density, improved Ru dispersion, and strong Ru-O-Ce interactions, collectively promoting N_2 activation, hydrogen transfer, and suppressing Ru aggregation.

Ru loading effect

To better understand how Ru particle size influences N_2 dissociation, it's helpful to revisit the recent study by Yanliang Zhou *et al.*[100]. Their findings clearly indicate that smaller Ru nanoparticles, specifically in $Ru/BaCeO_3$ systems, promote the generation of Ce^{3+} species and O_v. These vacancies enhance the electron transfer to Ru sites, thereby facilitating N_2 dissociation. Additionally, the structure-sensitive nature of NH_3 synthesis under mild conditions was emphasized by Peng *et al.*[101]. Their work shows that even subtle changes in Ru structure can significantly alter catalytic activity. Specifically, as Ru particle size decreases, the proportion of low-coordinated corner sites increases, while terrace site populations decline. This geometric evolution alters the electronic structure of Ru metal particles, effectively reducing the catalyst's work function (ϕ_{cat}). This reduction enhances electron transfer from Ru d-orbitals to N_2, promoting N_2 activation and subsequent N-H bond formation. Furthermore, isotopic labeling experiments combined with DRIFTS can shed light on the pool of N-containing intermediates and the underlying reaction mechanism, whether associative or dissociative. This is particularly relevant, as the Ru particle size can critically influence the mechanism. Larger Ru particles (> 2 nm) tend to follow a dissociative pathway[102], whereas atomically dispersed Ru favors an associative mechanism[18,19]. Smaller Ru sizes, with higher dispersion, also support hydrogen spillover to the support or interface, leading to the formation of O_v-H species. These can trap hydrogen and help mitigate H-poisoning effects on Ru[103], which typically occur under reaction conditions. Previous research[104] has indicated that Ru dispersion diminishes within the range of 1%-5% Ru, with optimal loading observed around 3.5%. Additionally, another study by Li *et al.*[105] showed that catalytic activity has no significant improvement beyond 4% Ru loading. To further support the role of Ru particle size and its impact on catalytic performance, the Ru loading was systematically varied from 0.2 to 1 wt.% over CeO_2. This variation allowed us to tune the Ru nanoparticle size from 0.9 to 1.06 and 1.2 nm, respectively. At 10 bar and 400 °C [Figure 9A], the NH_3 synthesis activity of the Ru/CeO_2 catalysts displayed a clear dependence on Ru loading. The $0.5Ru/CeO_2$ catalyst exhibited the highest NH_3 production rate of 2,811 ± 47.5 μmol g^{-1} h^{-1}, followed by $1Ru/CeO_2$ with 2,080 ± 48.1 μmol g^{-1} h^{-1}, and $0.2Ru/CeO_2$ with 1,615 ± 118.8 μmol g^{-1} h^{-1}. The CeO_2 support alone showed negligible activity under the same conditions. This trend highlights the importance of optimizing Ru dispersion and particle size, with 0.5 wt% Ru offering the most favorable balance for efficient NH_3 production at moderate pressures. The NH_3 synthesis activity at 400 °C and 10 bar, showed a non-linear trend: $0.2Ru/CeO_2 < 0.5Ru/CeO_2 > 1Ru/CeO_2$, indicating an optimum size and dispersion effect of Ru nanoparticles. The catalyst with 0.5 wt% Ru loading, possessing an average Ru particle size of approximately 1.02 nm, exhibited the best activity. This directly aligns with literature findings (Peng *et al.*[101], Zhou *et al.*[100]) that highlight the structure-sensitive nature of NH_3 synthesis, where small changes in nanoparticle size can shift the balance between active corner sites and less active terrace sites. Beyond just size effects, the interaction between Ru metal particles and the CeO_2 support also played a crucial role. Raman spectroscopy revealed an increase in O_v upon Ru incorporation, while H_2-TPR experiments confirmed enhanced reducibility of CeO_2. This was attributed to hydrogen spillover from Ru to the support, which facilitates the generation of O_v-H species, known to mitigate H-poisoning and support better N_2 activation. The above induce the following synergistic effects: optimized Ru size (~1.02 nm), increased oxygen vacancy concentration, and H-spillover-enhanced support activation, thus leading to collectively boosted NH_3 synthesis rates beyond what was achieved by CeO_2 standalone.

Effect of pressure

To investigate the effect of reaction pressure on the NH_3 synthesis activity, a series of nRu/CeO_2 catalysts with varying Ru loadings (0.2-1 wt%) were tested under pressures ranging from 10 to 50 bar and 400 °C and is shown in Figure 9A. According to Le Chatelier's principle[106], any change in system pressure will shift the equilibrium to counteract that change. For the ammonia synthesis reaction, $N_2(g) + 3H_2(g) \rightleftharpoons 2NH_3(g)$, an increase in pressure shifts the equilibrium toward the formation of ammonia, as the product side contains

fewer gas molecules. This theoretical understanding is consistent with our experimental findings, where an increase in reaction pressure from 10 to 50 bar led to a significant enhancement in NH_3 production rates across all *n*Ru/CeO_2 catalysts. The 0.5Ru/CeO_2 catalyst exhibited the highest activity, with NH_3 production reaching 4,665 μmol g^{-1} h^{-1} at 50 bar, highlighting its optimal balance of Ru loading and dispersion. The enhanced performance is not only attributed to the pressure-driven equilibrium shift but also to the catalyst's finely tuned Ru nanoparticle size (~1.02 nm), which promotes effective N_2 activation. On the other hand, catalysts with either lower (0.2 wt%) or higher (1-2 wt%) Ru loadings showed inferior performance due to insufficient active sites or excessive particle growth, respectively. These results emphasize that, while high pressure thermodynamically favors NH_3 formation, the structural and electronic properties of the catalyst play an equally critical role in achieving high catalytic efficiency.

Prolong stream effect

The catalyst with the best performance (0.5Ru/CeO_2) was selected for a prolonged stability study for 45 h time on stream. As shown in Figure 9B, the catalytic activity initially exhibited a slight increase during the early stages of the reaction. This behavior is likely attributed to the activation of the catalyst surface (exposure of some active sites) as it reaches its optimal working state under reaction conditions. Following this activation phase, the activity stabilized, indicating the catalyst maintained consistent performance throughout the prolonged study. This stability demonstrates that the catalyst is robust over extended periods and resistant to common deactivation pathways. Importantly, no signs of sintering (agglomeration of Ru particles) or hydrogen poisoning of the Ru active sites were observed. This confirms the catalyst's ability to retain its structural integrity and chemical functionality under prolonged reaction conditions, making it a promising candidate for long-term industrial applications. The catalyst maintained a stable NH_3 synthesis activity at 50 bar, 400 °C, and 10,000 mL $g^{-1}h^{-1}$.

NH_3 catalytic cracking performance

Given the high reversibility of NH_3 synthesis, we also evaluated the applicability of the *n*Ru/CeO_2 catalysts in NH_3 cracking at 350-550 °C and 1 bar. NH_3 cracking ($2NH_3 \rightarrow 3H_2+N_2$, ΔH = 92.44 kJ/mol) involves the cleavage of N-H bonds followed by the recombination of nitrogen and hydrogen atoms to form N_2 and H_2 gases[112]. As an endothermic reaction, its catalytic efficiency is highly dependent on temperature. The influence of temperature on NH_3 conversion% over the *n*Ru/CeO_2 catalysts is presented in Figure 9C. Within the range of 300 to 550 °C, NH_3 conversion steadily increases with temperature across all *n*Ru/CeO_2 catalysts. Notably, the 0.5Ru/CeO_2 catalyst exhibits the highest activity, achieving an impressive 93% NH_3 conversion at 550 °C. At this temperature, the conversion follows the trend: 0.2Ru/CeO_2 (80%) < 1Ru/CeO_2 (87%) < 0.5Ru/CeO_2 (93%). A similar trend is observed in the hydrogen production rate at 550 °C, with 0.5Ru/CeO_2 reaching 25,282 μmol g^{-1} min^{-1}, outperforming both 0.2Ru/CeO_2 (21,832 μmol g^{-1} min^{-1}) and 1Ru/CeO_2 (23,784 μmol g^{-1} min^{-1}) as shown in Figure 9D. Remarkably, the 0.5Ru/CeO_2 catalyst demonstrates superior NH_3 conversion and a faster decomposition rate compared to previously reported Ru/CeO_2 catalysts with Ru nanoparticles. The enhanced catalytic performance of the *n*Ru/CeO_2 catalyst for NH_3 cracking can be attributed to several key factors. First, the increased concentration of oxygen vacancies (O_{vs}) in the catalyst plays a critical role in improving catalytic activity[10,107,108]. These O_v act as active sites for the adsorption and dissociation of N_2 and H_2, which are essential steps in the NH_3 cracking reaction. Raman and XPS analysis confirmed the higher O_v concentration, as indicated by the Raman spectroscopy, which correlates with improved catalytic efficiency. Additionally, the hydrogen spillover effect, observed through H_2-TPR analysis, further facilitates the NH_3 cracking process. The spillover effect allows for the migration of atomic hydrogen from the Ru nanoparticles to the CeO_2 support, thereby enhancing the cleavage of N-H bonds and improving the overall hydrogen production rate[109]. Moreover, the fine dispersion of Ru on the MOF-derived CeO_2 support, as confirmed by HR-TEM, ensures that a large surface area of Ru is available for the reaction, preventing agglomeration and maximizing the number of active sites[110]. These combined effects: higher

oxygen vacancy concentration, effective hydrogen spillover, and enhanced Ru dispersion contribute to the superior catalytic performance of the *n*Ru/CeO_2 catalyst, which outperforms previously reported Ru/CeO_2 catalysts in NH_3 cracking.

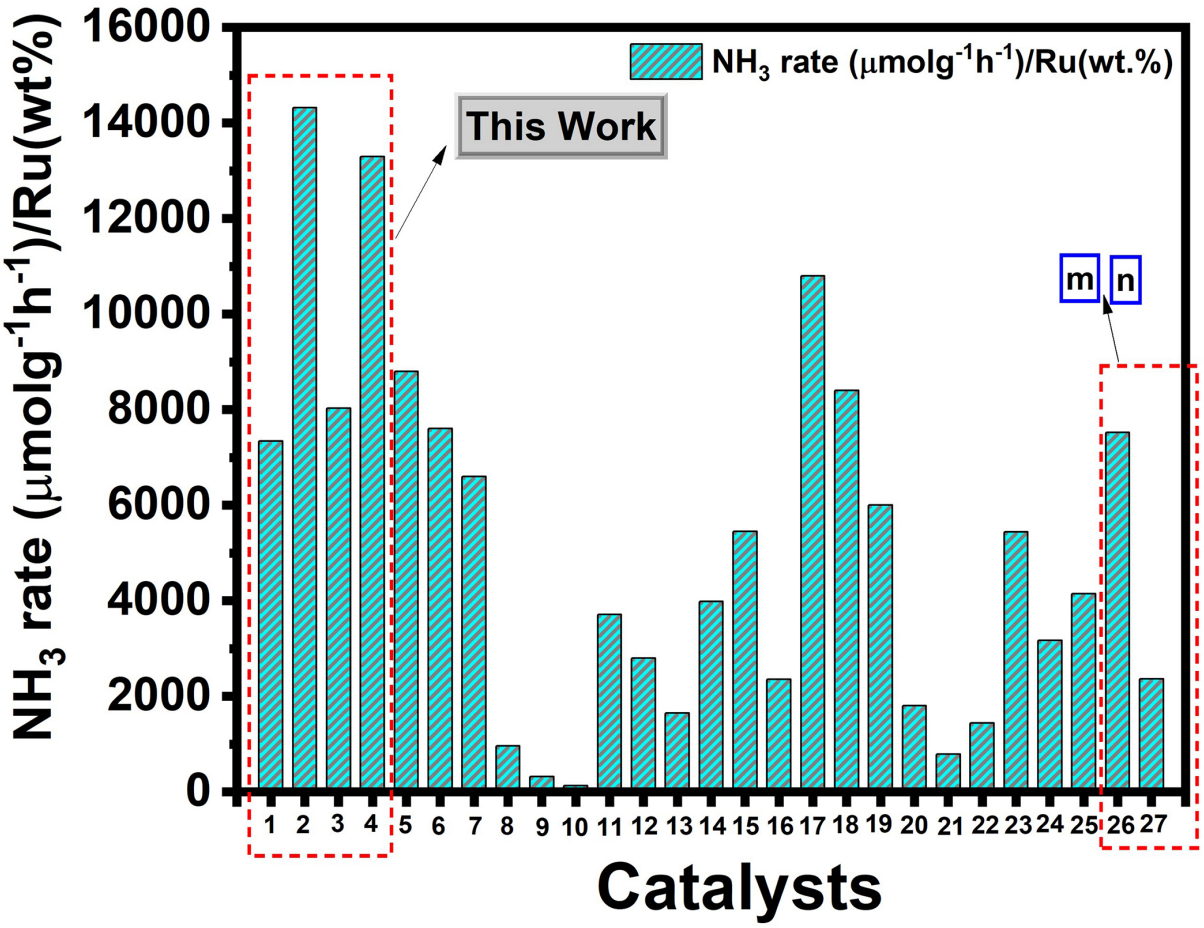

Figure 10. Comparison with the reported literature on Ru/CeO_2-based catalysts. *m*: similar compositions with KAAP catalysts; *n*: commercial Fe catalyst having similar compositions as Mittasch's catalyst.

When benchmarked against other reported Ru/CeO_2 systems with varying Ru weight loadings, our 0.5Ru/CeO_2 catalyst [Supplementary Table 3, Figure 10] demonstrated superior performance, further underscoring the importance of precise control over Ru particle size and metal-support interactions. These findings validate the previously discussed mechanism, where Ru size not only alters site populations and electronic structure (thus affecting work function and N_2 dissociation) but also determines the operative reaction pathway: associative or dissociative, especially near the critical ~1 nm (Ru particle size) threshold.

Post-catalytic study

The post-catalytic surface and structure characterization was performed after conducting the following tests: NH_3 synthesis, NH_3 cracking (300-550 °C), and the NH_3 synthesis stability test. The provided post-catalytic assessment results in the XRD [Figure 11A, Supplementary Table 4] and HRTEM images [Figure 11B-D] provide important insights into the structural changes and metal dispersion on *n*Ru/CeO_2 catalysts after the catalytic reaction for NH_3 synthesis and cracking. The XRD patterns show the characteristic peaks of CeO_2, indicating that the ceria support retains its fluorite structure after the catalytic reaction. The peaks observed at 28.4°, 33°, 47.4°, 56.3°, and 59°, 65.6°, 69.4°, 76.6°, and 79° correspond to the CeO_2 (111), (200), (220),

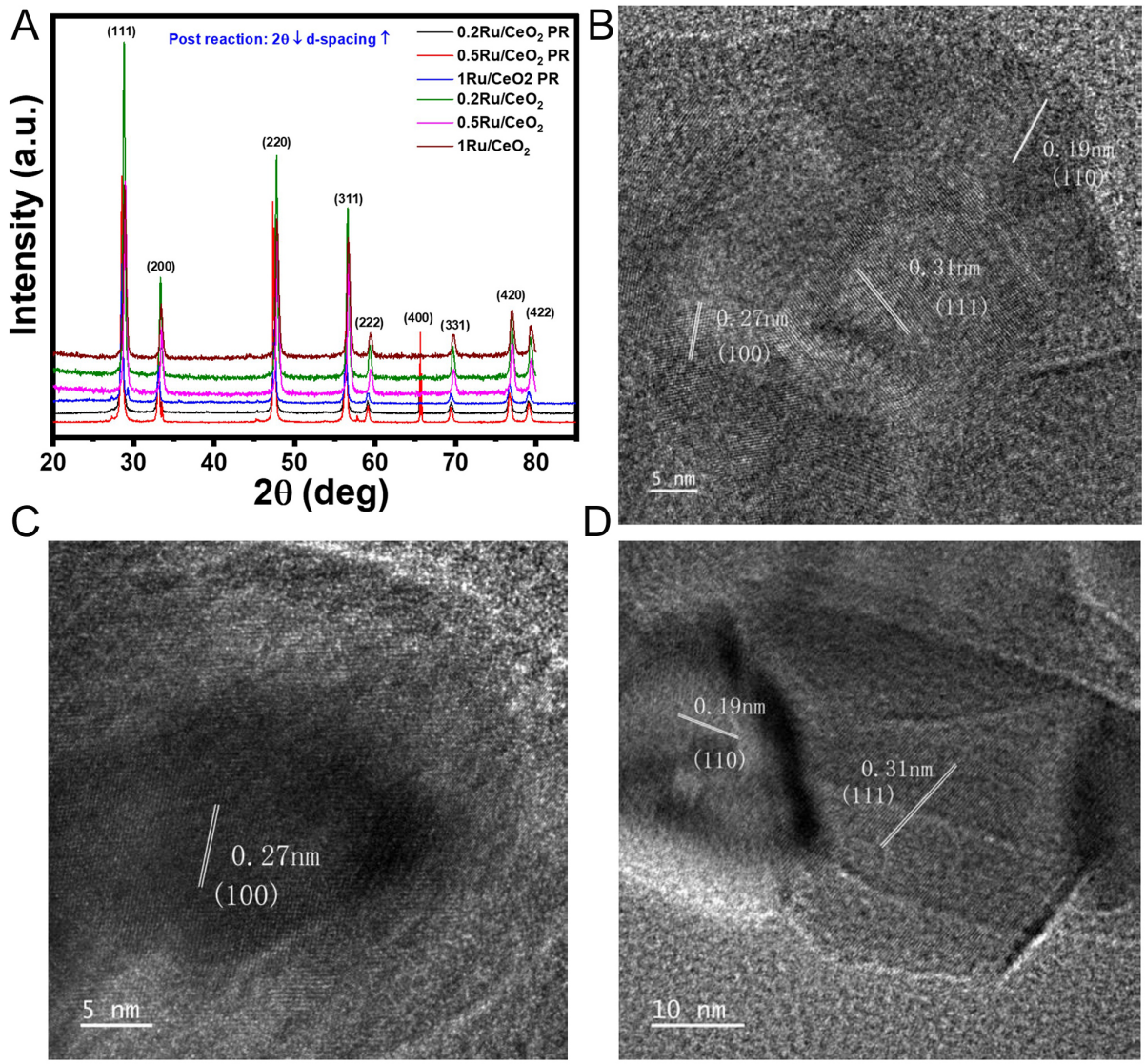

Figure 11. (A) XRD of CeO_2 support and *n*Ru/CeO_2 (*n* = 0.2, 0.5, and 1 wt%) before (reduced (under 10%H_2/Ar, 800 °C, 1 h)) and after catalytic activity test, and HRTEM of (B) 0.2Ru/CeO_2 (C), 0.5Ru/CeO_2, and (D) 1Ru/CeO_2 catalysts after catalytic activity test.

(311), (222), 400, (331), (420), and (422) planes, respectively. After the reaction, the CeO_2 diffraction peaks shift slightly to lower 2θ value, indicating increase in lattice parameters [Supplementary Table 4]. The increase in lattice spacing observed in the XRD studies is also observed in post catalytic HRTEM analyses, particularly the shift in the d-spacing corresponding to the characteristic CeO_2 plane (111) from 3.08 to 3.12 Å after the catalytic reaction, suggests that structural changes occurred in the catalyst during the NH_3 decomposition process. This change in lattice spacing could be attributed to the formation of oxygen vacancies in the CeO_2 support during the reaction. The creation of oxygen vacancies typically leads to local distortions in the crystal lattice[111], which can cause an expansion of the lattice as the ceria undergoes reduction. Furthermore, the interaction between the Ru nanoparticles and the CeO_2 support might contribute to this lattice expansion[87,112]. The Ru species, especially when atomically dispersed or present as small clusters, can influence the electronic environment of the CeO_2 support, potentially weakening the Ce-O bonds and facilitating the formation of vacancies[113]. This expansion of the lattice upon oxygen vacancy formation is consistent with previous studies, where CeO_2 lattice is observed to expand upon reduction due to the transformation of Ce^{4+}(0.94 Å) to Ce^{3+} (1.04 Å)[114,115]. However, the post-reaction XRD data confirms that the CeO_2 support remains stable, and there are no significant signs of phase segregation or crystallite growth for Ru, indicating a well-dispersed catalyst.

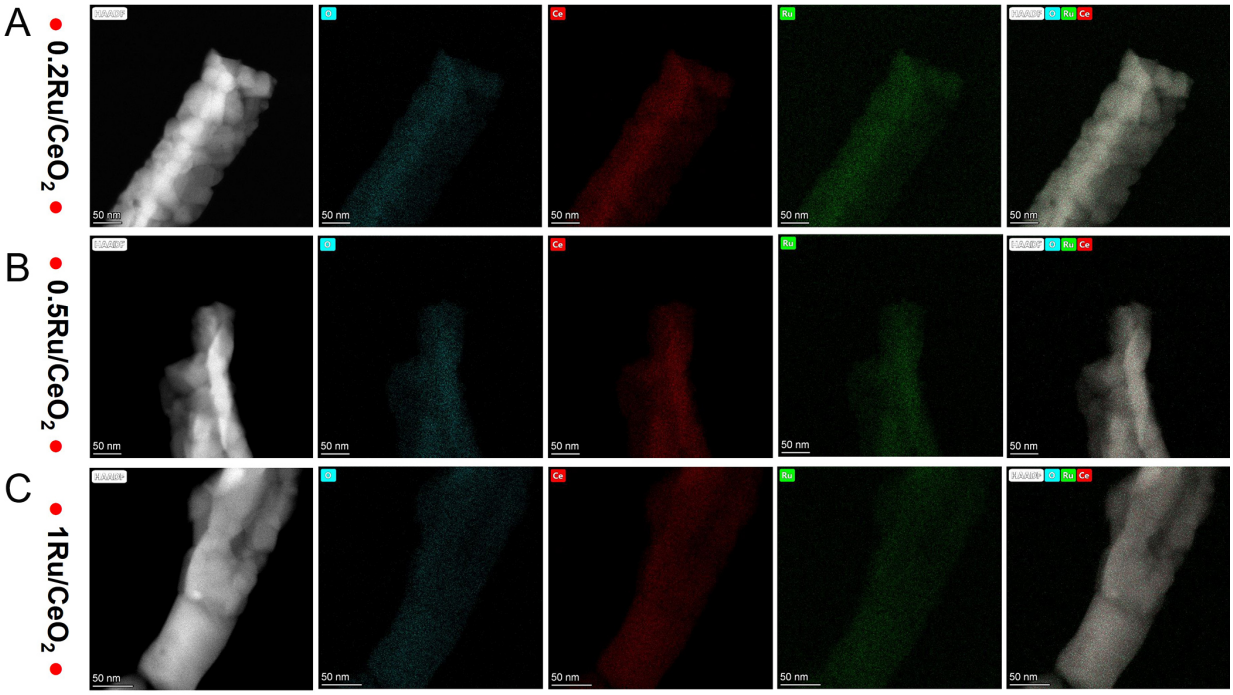

Figure 12. STEM-HAADF image and elemental mapping of the selected area of *n*Ru/CeO_2, (A) 0.2Ru, (B) 0.5Ru, and (C) 1Ru catalyst after catalytic activity test. Ru (Green), Ce (Red), O (Blue), Ce-O-Ru (RBG).

The post-catalytic HRTEM images [Supplementary Figure 10A-C] reveal that the *n*Ru/CeO_2 catalysts are rod-shaped, with widths ranging from 60 to 70 nm and lengths of approximately 1 μm. The lattice fringe spacings observed are 0.19, 0.27, and 0.32 nm, which correspond to the (220), (200), and (111) facets of CeO_2[107]. Notably, no identifiable Ru nanoclusters were observed on the surfaces of the *n*Ru/CeO_2 catalysts, suggesting that the Ru species are likely dispersed at the subnanometer or even single-atom level[116].

The EDX mapping results [Figure 12A-C] further confirm the homogeneous distribution of Ru species across the entire nanostructure. High-magnification HAADF-STEM images reveal no clusters, indicating that Ru does not exist as clusters or particles in the observed regions[117].

CONCLUSIONS

This work demonstrates the rational design of MOF-derived Ru/CeO_2 catalysts for efficient NH_3 synthesis and decomposition. Catalytic performance strongly depends on Ru loading and particle size, with 0.5 wt.% Ru/CeO_2 showing optimal activity, stability, and resistance to sintering. The enhanced performance arises from abundant oxygen vacancies and strong Ru-CeO_2 interfacial interactions, which promote H_2 activation and N_2 dissociation. Raman and *in-situ* XPS confirm the key role of oxygen vacancies in facilitating N_2 activation. These findings provide valuable structural insights for optimizing Ru-based catalysts toward sustainable energy applications.

DECLARATIONS

Authors' contributions

Writing - original draft, writing - review & editing, methodology, investigation, formal analysis, data curation: Singh, S.
Writing - review & editing, investigation, data curation: Kim, S. J.
Writing - review & editing, supervision, resources, formal analysis: Yavuz, C. T.
Formal analysis, investigation: Komarala, E. P.
Writing -review & editing, investigation, resources: Tan, M.

Writing - review & editing, validation, supervision, resources, project administration, funding acquisition, conceptualization: Polychronopoulou, K.

Availability of data and materials

Some results of supporting the study are presented in the Supplementary Materials. Other raw data that supports the findings of this study are available from the corresponding author upon reasonable request.

AI and AI-assisted tools statement

Not applicable.

Financial support and sponsorship

The authors acknowledge the financial support from Khalifa University through the Center for Catalysis and Separations (CeCaS), grant RC2-2018-024.

Conflicts of interest

All authors declared that there are no conflicts of interest.

Ethical approval and consent to participate

Not applicable.

Consent for publication

Not applicable.

Supplementary Materials

Supplementary Materials

REFERENCES

1. He, Y.; Guan, B.; Zhuang, Z.; et al. Advances in ammonia (NH_3) adsorption and storage: materials, mechanisms, and applications. *Adsorption* **2025**, *31*, 48. DOI
2. Hassan, Q.; Algburi, S.; Sameen, A. Z.; Jaszczur, M.; Salman, H. M. Hydrogen as an energy carrier: properties, storage methods, challenges, and future implications. *Environ. Syst. Decis.* **2023**, *44*, 327-50. DOI
3. Marakatti, V. S.; Gaigneaux, E. M. Recent advances in heterogeneous catalysis for ammonia synthesis. *ChemCatChem* **2020**, *12*, 5838-57. DOI
4. Lim, J.; Fernández, C. A.; Lee, S. W.; Hatzell, M. C. Ammonia and nitric acid demands for fertilizer use in 2050. *ACS. Energy. Lett.* **2021**, *6*, 3676-85. DOI
5. Macfarlane, D. R.; Cherepanov, P. V.; Choi, J.; et al. A roadmap to the ammonia economy. *Joule* **2020**, *4*, 1186-205. DOI
6. Ma, Y.; Lan, G.; Fu, W.; et al. Role of surface defects of carbon nanotubes on catalytic performance of barium promoted ruthenium catalyst for ammonia synthesis. *J. Energy. Chem.* **2020**, *41*, 79-86. DOI
7. Singh, S.; Mohammed, A. K.; Alhammadi, A. A.; Shetty, D.; Polychronopoulou, K. Hypes and hopes on the materials development strategies to produce ammonia at mild conditions. *Int. J. Hydrogen. Energy.* **2023**, *48*, 34700-39. DOI
8. Othman, A.; Gowda, A.; Andreescu, D.; et al. Two decades of ceria nanoparticle research: structure, properties and emerging applications. *Mater. Horiz.* **2024**, *11*, 3213-66. DOI
9. Liu, H.; Zhang, R.; Liu, S.; Liu, G. CeO_2/Ni inverse catalyst as a highly active and stable Ru-free catalyst for ammonia decomposition. *ACS. Catal.* **2024**, *14*, 9927-39. DOI
10. Teng, B.; Ma, C.; Chen, J.; et al. Ru dispersed on oxygen-defect-rich CeO_2 nanorods for ammonia decomposition. *ACS. Appl. Nano. Mater.* **2024**, *7*, 15012-24. DOI
11. Zhu, X.; Liu, S.; Li, Y.; et al. Redox CeO_2 substituted Na_2WO_4-Mn catalyst for high-throughput chemical looping oxidative coupling of methane. *Appl. Catal. B. Environ. Energy.* **2025**, *367*, 125108. DOI
12. Liu, B.; Pan, Y.; Han, Z.; et al. Interplay of structural properties and redox behavior in CeO_2 nanoparticles: impact on reactivity and bioavailability. *Environ. Sci. Technol.* **2025**, *59*, 4641-51. DOI

13. Parastaev, A.; Muravev, V.; Huertas, Osta. E.; et al. Boosting CO_2 hydrogenation via size-dependent metal-support interactions in cobalt/ceria-based catalysts. *Nat. Catal.* **2020**, *3*, 526-33. DOI
14. Buhori, A.; Choi, J.; Lee, H.; et al. Effect of CeO_2 morphology and Ru impregnation method on CH4 selectivity reduction in polyethylene waste conversion to liquid fuels and lubricants. *Chem. Eng. J.* **2024**, *499*, 156097. DOI
15. Wei, J.; Sun, Y.; Ma, Y.; et al. Tailored metal-oxygen defect engineering to modulate catalytic interaction of ultra-low Ru supported morphology-oriented CeO_2 for hydrogenolysis of lignin-derived phenols. *Chem. Eng. J.* **2025**, *509*, 161199. DOI
16. Yamazaki, K.; Goto, Y.; Kikugawa, M.; et al. Effect of support morphology on the ammonia synthesis activity of Ru/CeO_2-based catalysts. *Int. J. Hydrogen. Energy.* **2024**, *94*, 406-19. DOI
17. Xie, B.; Wang, Z.; Zhang, X.; et al. Morphology effect of cerium dioxide on the catalytic performance of Ru/CeO_2 catalyst for the oxidation of different CVOCs. *Sep. Purif. Technol.* **2024**, *345*, 127428. DOI
18. Wang, J.; Zhang, H.; Shi, L.; et al. Morphological effects of cerium oxide on photothermal synergistic catalytic degradation of toluene. *Sep. Purif. Technol.* **2026**, *380*, 135271. DOI
19. Ma, Z.; Zhao, S.; Pei, X.; Xiong, X.; Hu, B. New insights into the support morphology-dependent ammonia synthesis activity of Ru/CeO_2 catalysts. *Catal. Sci. Technol.* **2017**, *7*, 191-9. DOI
20. Li, W. Q.; Xu, M.; Chen, J. S.; Ye, T. N. Enabling sustainable ammonia synthesis: from nitrogen activation strategies to emerging materials. *Adv. Mater.* **2024**, *36*, 2408434. DOI
21. Zhang, L.; Zhou, M.; Wang, A.; Zhang, T. Selective Hydrogenation over supported metal catalysts: from nanoparticles to single atoms. *Chem. Rev.* **2019**, *120*, 683-733. DOI PubMed
22. Sarma, B. B.; Kim, J.; Amsler, J.; et al. One-pot cooperation of single-atom Rh and Ru Solid catalysts for a selective tandem olefin isomerization-hydrosilylation process. *Angew. Chem. Int. Ed.* **2020**, *59*, 5806-15. DOI PubMed PMC
23. Ansari, M. Z.; Habib, F.; Gupta, J.; et al. Frontiers in metal-organic frameworks: innovative nanomaterials for next-generation supercapacitors. *Adv. Compos. Hybrid. Mater.* **2024**, *7*, 215. DOI
24. Zulfiqar, A.; Miao, B.; Khan, F.; et al. Metal-organic framework (MOF)-based catalysts for sustainable energy technologies: a review. *Langmuir* **2025**, *41*, 24049-77. DOI
25. Sousa, A.; Rendon, Patino. A.; Garzon, Tovar. L.; Mateo, D.; Gascon, J.; Bavykina, A. Ammonia decomposition via MOF-derived photothermal catalysts. *ChemSusChem* **2024**, *18*, e202401896. DOI PubMed
26. Wu, W.; Yao, W.; Liu, Y.; Xi, S.; Zhang, T. Efficient hydrogen production from ammonia using Ru nanoparticles on Ce-based metal-organic framework (MOF)-derived CeO_2 with oxygen vacancies. *Molecules* **2025**, *30*, 2301. DOI PubMed PMC
27. Song, Q.; Yin, X.; Zhang, H. Ni-MOF-74 derived carbon-based Ni catalysts for efficient catalytic ammonia synthesis via pulsed DBD plasma. *Plasma. Processes. Polym.* **2024**, *22*, 2400173. DOI
28. Li, S.; Wang, N.; Yue, Y.; Wang, G.; Zu, Z.; Zhang, Y. Copper doped ceria porous nanostructures towards a highly efficient bifunctional catalyst for carbon monoxide and nitric oxide elimination. *Chem. Sci.* **2015**, *6*, 2495-500. DOI PubMed PMC
29. Gandhi, H.; Graham, G.; Mccabe, R. Automotive exhaust catalysis. *J. Catal.* **2003**, *216*, 433-42. DOI
30. Porta, A.; Falbo, L.; Visconti, C. G.; Lietti, L.; Bassano, C.; Deiana, P. Synthesis of Ru-based catalysts for CO_2 methanation and experimental assessment of intraporous transport limitations. *Catal. Today.* **2020**, *343*, 38-47. DOI
31. Hussain, J.; Lin, K.; Chowdhury, S.; Hussain, A. Synthesis and characterization of hexagonal ceria-BTC microrods for methanol decomposition. *J. Taiwan. Inst. Chem. Eng.* **2024**, *159*, 105486. DOI
32. Borges, Serra. A. R.; Castro, De. Sousa. G.; De, Carvalho. Gomes. V.; et al. Enhancing photocatalytic tetracycline degradation through the fabrication of high surface area CeO_2 from a cerium-organic framework. *RSC. Adv.* **2024**, *14*, 17507-18. DOI PubMed PMC
33. Zhao, Z.; Jiang, Q.; Wang, Q.; et al. Effect of rutile content on the catalytic performance of Ru/TiO_2 catalyst for low-temperature CO_2 methanation. *ACS. Sustain. Chem. Eng.* **2021**, *9*, 14288-96. DOI
34. Li, Y.; Zhang, L. A.; Qin, Y.; et al. Crystallinity dependence of ruthenium nanocatalyst toward hydrogen evolution reaction. *ACS. Catal.* **2018**, *8*, 5714-20. DOI
35. Sivan, S. E.; Kang, K. H.; Han, S. J.; et al. Facile MOF-derived one-pot synthetic approach toward Ru single atoms, nanoclusters, and nanoparticles dispersed on CeO_2 supports for enhanced ammonia synthesis. *J. Catal.* **2022**, *408*, 316-28. DOI
36. Shannon, R. D. Revised effective ionic radii and systematic studies of interatomic distances in halides and chalcogenides. *Acta. Cryst. A.* **1976**, *32*, 751-67. DOI
37. Sharma, S.; Hu, Z.; Zhang, P.; Mcfarland, E. W.; Metiu, H. CO_2 methanation on Ru-doped ceria. *J. Catal.* **2011**, *278*, 297-309. DOI
38. Singh, P.; Hegde, M. S. $Ce_xRu_xO_{2-\delta}$ (x = 0.05, 0.10): a new high oxygen storage material and Pt, Pd-free three-way catalyst. *Chem. Mater.* **2009**, *21*, 3337-45. DOI

39. Carrillo, A. J.; Navarrete, L.; Laqdiem, M.; Balaguer, M.; Serra, J. M. Boosting methane partial oxidation on ceria through exsolution of robust Ru nanoparticles. *Mater. Adv.* **2021**, *2*, 2924-34. DOI
40. Pandit, N. A.; Alshehri, S. M.; Ahmad, T. CeO_2/ZrO_2 p-n heterojunction nanostructures for efficient NO_2 gas sensing. *J. Alloys. Compd.* **2024**, *1004*, 175782. DOI
41. Iqbal, M. W.; Yu, Y.; Simakov, D. S. Enhancing the surface area stability of the cerium oxide reverse water gas shift nanocatalyst via reverse microemulsion synthesis. *Catal. Today.* **2023**, *407*, 230-43. DOI
42. Kang, W.; Ozgur, D. O.; Varma, A. Solution combustion synthesis of high surface area CeO_2 nanopowders for catalytic applications: reaction mechanism and properties. *ACS. Appl. Nano. Mater.* **2018**, *1*, 675-85. DOI
43. Zaidi, R.; Khan, S. U.; Farooqi, I. H.; et al. Performance, isotherm, kinetics and mechanism of simultaneous removal of Cr(VI), Cu(II) and F ions by CeO_2-MgO binary oxide nanomaterials. *Sci. Rep.* **2025**, *15*, 1431. DOI PubMed PMC
44. López-Rodríguez, S.; Davó-Quiñonero, A.; Bailón-García, E.; Lozano-Castelló, D.; Bueno-López, A. Effect of Ru loading on Ru/CeO_2 catalysts for CO_2 methanation. *Mol. Catal.* **2021**, *515*, 111911. DOI
45. Feng, Q.; Zou, J.; Wang, Y.; et al. Influence of surface oxygen vacancies and ruthenium valence state on the catalysis of pyrochlore oxides. *ACS. Appl. Mater. Interfaces.* **2020**, *12*, 4520-30. DOI
46. Zhou, S.; Ban, T.; Li, T.; et al. Defect engineering in Ce-based metal-organic frameworks toward enhanced catalytic performance for hydrogenation of dicyclopentadiene. *ACS. Appl. Mater. Interfaces.* **2024**, *16*, 38177-87. DOI
47. Giri, G.; Verploegen, E.; Mannsfeld, S. C. B.; et al. Tuning charge transport in solution-sheared organic semiconductors using lattice strain. *Nature* **2011**, *480*, 504-8. DOI
48. Dave, M.; Dalela, S.; Kumar, S.; Alvi, P. A. Defect induced structural and Raman study of Nd-doped CeO_2 nanomaterials. *AIP. Conf. Proc.* **2020**, *2265*, 030108. DOI
49. Bezkrovnyi, O. S.; Kraszkiewicz, P.; Ptak, M.; Kepinski, L. Thermally induced reconstruction of ceria nanocubes into zigzag {111}-nanofacetted structures and its influence on catalytic activity in CO oxidation. *Catal. Commun.* **2018**, *117*, 94-8. DOI
50. Angermann, M.; Jakopic, G.; Prietl, C.; Griesser, T.; Reichmann, K.; Deluca, M. Highly conductive RuO_2 thin films from novel facile aqueous chemical solution deposition. *J. Sol-Gel. Sci. Technol.* **2023**, *108*, 575-87. DOI
51. Yao, X.; Zhang, L.; Li, L.; et al. Investigation of the structure, acidity, and catalytic performance of $CuO/Ti_{0.95}Ce_{0.05}O_2$ catalyst for the selective catalytic reduction of NO by NH_3 at low temperature. *Appl. Catal. B. Environ.* **2014**, *150-151*, 315-29. DOI
52. Wu, Z.; Li, M.; Howe, J.; Meyer, H. M.; Overbury, S. H. Probing defect sites on CeO_2 nanocrystals with well-defined surface planes by Raman spectroscopy and O_2 adsorption. *Langmuir* **2010**, *26*, 16595-606. DOI
53. Dai, Q.; Huang, H.; Zhu, Y.; et al. Catalysis oxidation of 1,2-dichloroethane and ethyl acetate over ceria nanocrystals with well-defined crystal planes. *Appl. Catal. B. Environ.* **2012**, *117-8*, 360-8. DOI
54. Chen, H. First-principles study of CO adsorption and oxidation on Ru-doped CeO_2(111) surface. *J. Phys. Chem. C.* **2012**, *116*, 6239-46. DOI
55. Huang, H.; Dai, Q.; Wang, X. Morphology effect of Ru/CeO_2 catalysts for the catalytic combustion of chlorobenzene. *Appl. Catal. B. Environ.* **2014**, *158-9*, 96-105. DOI
56. Zhang, X.; Zheng, J.; Boch, F. J.; Nickl, S.; Köhler, K. Decomposition of N_2O by ruthenium catalysts - RuO_2 as active phase on non-reducible supports. *ChemCatChem* **2024**, *16*, e202400347. DOI
57. Mi, R.; Li, D.; Hu, Z.; Yang, R. T. Morphology effects of CeO_2 nanomaterials on the catalytic combustion of toluene: a combined kinetics and diffuse reflectance infrared fourier transform spectroscopy study. *ACS. Catal.* **2021**, *11*, 7876-89. DOI
58. Costa Zonetti P, Landers R, Cobo AJG. Thermal treatment effects on the Ru/CeO_2 catalysts performance for partial hydrogenation of benzene. *Appl. Surf. Sci.* **2008**, *254*, 6849-53. DOI
59. Kim, H.; Yang, S.; Lim, Y. H.; Lee, J.; Ha, J.; Kim, D. H. Enhancement in the metal efficiency of Ru/TiO_2 catalyst for guaiacol hydrogenation via hydrogen spillover in the liquid phase. *J. Catal.* **2022**, *410*, 93-102. DOI
60. Li, W.; Liu, P.; Niu, R.; Li, J.; Wang, S. Influence of CeO_2 supports prepared with different precipitants over Ru/CeO_2 catalysts for ammonia synthesis. *Solid. State. Sci.* **2020**, *99*, 105983. DOI
61. Sun, Y.; Xue, Z.; Liu, Q.; et al. Modulating electronic structure of metal-organic frameworks by introducing atomically dispersed Ru for efficient hydrogen evolution. *Nat. Commun.* **2021**, *12*, 1369. DOI PubMed PMC
62. Villarroel-rocha, J.; Gil, A. Modeling the temperature-programmed reduction of metal oxide catalysts by considering the particle-size distribution effect. *Chem. Eng. J.* **2024**, *487*, 150722. DOI
63. Unutulmazsoy, Y.; Cancellieri, C.; Lin, L.; Jeurgens, L. P. Reduction of thermally grown single-phase CuO and Cu_2O thin films by in-situ time-resolved XRD. *Appl. Surf. Sci.* **2022**, *588*, 152896. DOI

64. Chen, J.; Ni, J.; Xu, H.; He, G.; Chen, H. Mechanism and research progress of hydrogen spillover in hydrogen evolution reaction. *J. Alloys. Compd.* **2024**, *1004*, 175883. DOI
65. Lee, S.; Kim, H.; Ryoo, R.; Park, J. Y.; Choi, M. Hydrogen spillover in nonreducible oxides: mechanism and catalytic utilization. *Nano. Res.* **2022**, *15*, 10357-65. DOI
66. Li, Y.; Li, L.; Xu, S.; et al. Hydrogen spillover mechanism at the metal-metal interface in electrocatalytic hydrogenation. *Angew. Chem. Int. Ed.* **2024**, *63*, e202407810. DOI
67. Li, Y.; Chen, S.; Li, K.; et al. Plasma-assisted ammonia synthesis over La_2O_3 modified by RF discharge: effect of oxygen vacancies on N_2 adsorption and associative mechanism. *ACS. Sustain. Chem. Eng.* **2024**, *12*, 11728-38. DOI
68. Luo, S.; Liu, Y.; Guo, L.; et al. Plasma-derived hydrogen radical-mediated N_2 activation for mild ammonia synthesis: insights into the importance of oxygen vacancies in the reaction mechanism. *J. Mater. Chem. A.* **2025**, *13*, 30546-53. DOI
69. Zhu, H.; Wang, C.; He, Y.; et al. Oxygen vacancies engineering in electrocatalysts nitrogen reduction reaction. *Front. Chem.* **2022**, *10*, 1039738. DOI PubMed PMC
70. Wang, H.; Li, X.; Ruan, Q.; Tang, J. Ru and RuO_x decorated carbon nitride for efficient ammonia photosynthesis. *Nanoscale* **2020**, *12*, 12329-35. DOI
71. Polychronopoulou, K.; Alkhoori, S.; Albedwawi, S.; et al. Decoupling the chemical and mechanical strain effect on steering the CO_2 activation over CeO_2-based oxides: an experimental and DFT approach. *ACS. Appl. Mater. Interfaces.* **2022**, *14*, 33094-119. DOI PubMed PMC
72. Jiang, P.; Zhang, L.; Liu, X.; et al. Tuning oxidant and antioxidant activities of ceria by anchoring copper single-site for antibacterial application. *Nat. Commun.* **2024**, *15*, 1010. DOI PubMed PMC
73. Siakavelas, G.; Charisiou, N.; Alkhoori, S.; et al. Highly selective and stable nickel catalysts supported on ceria promoted with Sm_2O_3, Pr_2O_3 and MgO for the CO_2 methanation reaction. *Appl. Catal. B. Environ.* **2021**, *282*, 119562. DOI
74. Isaacs, M. A.; Drivas, C.; Lee, R.; Palgrave, R.; Parlett, C. M.; Morgan, D. J. XPS surface analysis of ceria-based materials: experimental methods and considerations. *Appl. Surface. Sci. Adv.* **2023**, *18*, 100469. DOI
75. Elmutasim, O.; Hussien, A. G.; Sharan, A.; et al. Evolution of oxygen vacancy sites in ceria-based high-entropy oxides and their role in N_2 activation. *ACS. Appl. Mater. Interfaces.* **2024**, acsami.3c16521. DOI
76. Xie, C.; Yan, D.; Li, H.; et al. Defect chemistry in heterogeneous catalysis: recognition, understanding, and utilization. *ACS. Catal.* **2020**, *10*, 11082-98. DOI
77. Peera, S. G.; Kim, S. W. Rare earth Ce/CeO_2 Electrocatalysts: role of high electronic spin state of Ce and Ce^{3+}/Ce^{4+} redox couple on oxygen reduction reaction. *Nanomaterials* **2025**, *15*, 600. DOI PubMed PMC
78. Kumar, A.; Lee, J.; Kim, M. G.; et al. Efficient nitrate conversion to ammonia on f-block single-atom/metal oxide heterostructure *via* local electron-deficiency modulation. *ACS. Nano.* **2022**, *16*, 15297-309. DOI
79. Zhang, Y.; Zhao, S.; Feng, J.; et al. Unraveling the physical chemistry and materials science of CeO_2-based nanostructures. *Chem* **2021**, *7*, 2022-59. DOI
80. Kang, L.; Wang, B.; Bing, Q.; et al. Adsorption and activation of molecular oxygen over atomic copper(I/II) site on ceria. *Nat. Commun.* **2020**, *11*, 4008. DOI PubMed PMC
81. Yang, X.; Han, R.; Shi, L.; et al. Dual-site engineering of La/Ti co-doped $BiFeO_3$ for enhanced visible-light photocatalytic degradation: synergistic effects and high stability. *J. Alloys. Compd.* **2025**, *1039*, 183239. DOI
82. Yu, W.; Wang, W.; Li, S.; et al. Construction of active site in a sintered copper-ceria nanorod catalyst. *J. Am. Chem. Soc.* **2019**, *141*, 17548-57. DOI
83. Yan, H.; Yang, C.; Shao, W.; et al. Construction of stabilized bulk-nano interfaces for highly promoted inverse CeO_2/Cu catalyst. *Nat. Commun.* **2019**, *10*, 3470. DOI PubMed PMC
84. Li, H.; Wang, H.; Gong, X.; et al. Multiple configurations of the two excess 4*f* electrons on defective CeO_2(111): origin and implications. *Phys. Rev. B.* **2009**, *79*, 193401. DOI
85. Holgado, J.; Munuera, G.; Espinós, J.; González-Elipe, A. XPS study of oxidation processes of CeO_x defective layers. *Appl. Surf. Sci.* **2000**, *158*, 164-71. DOI
86. Han, Z.; Liu, W.; Gao, Y. Advancing the understanding of oxygen vacancies in ceria: insights into their formation, behavior, and catalytic roles. *JACS. Au.* **2025**, *5*, 1549-69. DOI PubMed PMC
87. Feng, Z.; Guo, F.; Zhang, Y.; Ichikawa, T.; Zheng, J. Oxygen vacancies rich CeO_2 supported Ru catalyst for efficient hydrogenation of N-ethylcarbazole at mild temperature. *Appl. Catal. B. Environ. Energy.* **2025**, *366*, 125059. DOI

88. Lu, X.; Zhang, R.; Liu, Y.; et al. Oxygen vacancies and lattice distortion synergistically enhanced piezocatalysis of $CaZn_2(BO_3)_2$ for nonantibiotic pharmaceutical degradation. *ACS. Appl. Mater. Interfaces.* **2024**, *16*, 63692-702. DOI
89. Chou, M. Y.; Chelikowsky, J. R. Structural properties of the Ru(0001) surface. *Phys. Rev. B.* **1987**, *35*, 2124-7. DOI
90. Lin, B.; Liu, Y.; Heng, L.; et al. Morphology effect of ceria on the catalytic performances of Ru/CeO_2 catalysts for ammonia synthesis. *Ind. Eng. Chem. Res.* **2018**, *57*, 9127-35. DOI
91. Xu, B.; Xia, L.; Zhou, F.; et al. Enhancing electrocatalytic N_2 reduction to NH_3 by CeO_2 nanorod with oxygen vacancies. *ACS. Sustain. Chem. Eng.* **2019**, *7*, 2889-93. DOI
92. Yang, X.; Tian, Y.; Mukherjee, S.; et al. Constructing oxygen vacancies via engineering heterostructured Fe_3C/Fe_3O_4 catalysts for electrochemical ammonia synthesis. *Angew. Chem. Int. Ed.* **2023**, *62*, e202304797. DOI
93. Zhang, L.; Li, R.; Cui, L.; et al. Boosting photocatalytic ammonia synthesis performance over OVs-rich $Ru/W_{18}O_{49}$: insights into the roles of oxygen vacancies in enhanced hydrogen spillover effect. *Chem. Eng. J.* **2023**, *461*, 141892. DOI
94. Jiang, F.; Wang, S.; Liu, B.; et al. Insights into the influence of CeO_2 crystal facet on CO_2 hydrogenation to methanol over Pd/CeO_2 catalysts. *ACS. Catal.* **2020**, *10*, 11493-509. DOI
95. Aika, K.; Kumasaka, M.; Oma, T.; et al. Support and promoter effect of ruthenium catalyst. III. Kinetics of ammonia synthesis over various Ru catalysts. *Appl. Catal.* **1986**, *28*, 57-68. DOI
96. Fuller, J.; An, Q.; Fortunelli, A.; Goddard, W. A. Reaction mechanisms, kinetics, and improved catalysts for ammonia synthesis from hierarchical high throughput catalyst design. *Acc. Chem. Res.* **2022**, *55*, 1124-34. DOI PubMed
97. Li, H.; Shang, J.; Ai, Z.; Zhang, L. Efficient visible light nitrogen fixation with BiOBr nanosheets of oxygen vacancies on the exposed {001} facets. *J. Am. Chem. Soc.* **2015**, *137*, 6393-9. DOI
98. Hirakawa, H.; Hashimoto, M.; Shiraishi, Y.; Hirai, T. Photocatalytic conversion of nitrogen to ammonia with water on surface oxygen vacancies of Titanium dioxide. *J. Am. Chem. Soc.* **2017**, *139*, 10929-36. DOI
99. Lee, Y.; He, G.; Akey, A. J.; Si, R.; Flytzani-stephanopoulos, M.; Herman, I. P. Raman analysis of mode softening in nanoparticle $CeO_{2-\delta}$ and Au-$CeO_{2-\delta}$ during CO oxidation. *J. Am. Chem. Soc.* **2011**, *133*, 12952-5. DOI
100. Zhou, Y.; Wang, J.; Liang, L.; et al. Unraveling the size-dependent effect of Ru-based catalysts on Ammonia synthesis at mild conditions. *J. Catal.* **2021**, *404*, 501-11. DOI
101. Peng, X.; Chen, X.; Zhou, Y.; et al. Size-dependent activity of supported Ru catalysts for ammonia synthesis at mild conditions. *J. Catal.* **2022**, *408*, 98-108. DOI
102. Hinrichsen, O.; Rosowski, F.; Hornung, A.; Muhler, M.; Ertl, G. The kinetics of ammonia synthesis over Ru-based catalysts. *J. Catal.* **1997**, *165*, 33-44. DOI
103. Yao, Y.; Zhu, S.; Wang, H.; Li, H.; Shao, M. A spectroscopic study on the nitrogen electrochemical reduction reaction on gold and platinum surfaces. *J. Am. Chem. Soc.* **2018**, *140*, 1496-501. DOI
104. Rossetti, I.; Forni, L. Effect of Ru loading and of Ru precursor in Ru/C catalysts for ammonia synthesis. *Appl. Catal. A. Gen.* **2005**, *282*, 315-20. DOI
105. Li, Z. Ammonia synthesis on graphitic-nanofilament supported Ru catalysts. *J. Mol. Catal. A. Chem.* **2004**, *211*, 103-9. DOI
106. Wang, H.; Wu, Q.; Xiao, F. Design of zeolite-based catalysts by Le Chatelier's principle. *Appl. Catal. B. Environ. Energy*. **2025**, *379*, 125671. DOI
107. Shin, J.; Jung, U.; Kim, J.; et al. Elucidating the effect of Ce with abundant surface oxygen vacancies on $MgAl_2O_4$-supported Ru-based catalysts for ammonia decomposition. *Appl. Catal. B. Environ.* **2024**, *340*, 123234. DOI
108. Huang, C.; Yu, Y.; Tang, X.; et al. Hydrogen generation by ammonia decomposition over Co/CeO_2 catalyst: influence of support morphologies. *Appl. Surf. Sci.* **2020**, *532*, 147335. DOI
109. Su, Q.; Gu, L.; Yao, Y.; et al. Layered double hydroxides derived $Ni_x(Mg_yAl_2On)$ catalysts: enhanced ammonia decomposition by hydrogen spillover effect. *Appl. Catal. B. Environ.* **2017**, *201*, 451-60. DOI
110. Zhang, B.; Yang, J.; Mu, Y.; et al. Fabrication of highly dispersed Ru catalysts on CeO_2 for efficient C_3H_6 oxidation. *Environ. Sci. Technol.* **2024**, *58*, 19533-44. DOI
111. Rocha, L. S. R.; Aparecido, Ciola. Amoresi. R.; Duarte, T. M.; et al. Experimental and theoretical interpretation of the order/disorder clusters in CeO_2:La. *Appl. Surf. Sci.* **2020**, *510*, 145216. DOI
112. Ranasinghe, K. S.; Singh, R.; Leshchev, D.; Vasquez, A.; Stavitski, E.; Foster, I. Synthesis of nanoceria with varied ratios of Ce^{3+}/Ce^{4+} utilizing soluble borate glass. *Nanomaterials* **2022**, *12*, 2363. DOI PubMed PMC
113. Zheng, C.; Mao, D.; Xu, Z.; Zheng, S. Strong Ru-CeO_2 interaction boosts catalytic activity and stability of Ru supported on CeO_2 nanocube for soot oxidation. *J. Catal.* **2022**, *411*, 122-34. DOI

114. Castleton, C. W. M.; Kullgren, J.; Hermansson, K. Tuning LDA+U for electron localization and structure at oxygen vacancies in ceria. *J. Chem. Phys.* **2007**, *127*, 244704. DOI PubMed

115. Tomar, S.; Bhadoria, B. S.; Jeong, H.; Choi, J. H.; Lee, S.; Bhattacharjee, S. Single-atom Pd catalyst on a CeO_2 (111) surface for methane oxidation: activation barriers and reaction pathways. *J. Phys. Chem. C.* **2024**, *128*, 8580-9. DOI

116. Guo, Y.; Mei, S.; Yuan, K.; et al. Low-temperature CO_2 methanation over CeO_2-supported Ru single atoms, nanoclusters, and nanoparticles competitively tuned by strong metal-support interactions and H-spillover effect. *ACS. Catal.* **2018**, *8*, 6203-15. DOI

117. Wu, B.; Lin, T.; Yang, R.; et al. Ru single atoms for efficient chemoselective hydrogenation of nitrobenzene to azoxybenzene. *Green. Chem.* **2021**, *23*, 4753-61. DOI